

Hopf bifurcation and time periodic orbits with `pde2path` – algorithms and applications

Hannes Uecker

Institut für Mathematik, Universität Oldenburg, D26111 Oldenburg, hannes.uecker@uni-oldenburg.de

December 29, 2017, last updated: August 31, 2018

Abstract

We describe the algorithms used in the `Matlab` continuation and bifurcation package `pde2path` for Hopf bifurcation and continuation of branches of periodic orbits in systems of PDEs in 1, 2, and 3 spatial dimensions, including the computation of Floquet multipliers. We first test the methods on three reaction diffusion examples, namely a complex Ginzburg–Landau equation as a toy problem, a reaction diffusion system on a disk with rotational waves including stable spirals bifurcating out of the trivial solution, and a Brusselator system with interaction of Turing and Turing–Hopf bifurcations. Then we consider a system from distributed optimal control, which is ill-posed as an initial value problem and thus needs a particularly stable method for computing Floquet multipliers, for which we use a periodic Schur decomposition. The implementation details how to use `pde2path` on these problems are given in an accompanying tutorial, which also includes a number of further examples and algorithms, for instance on Hopf bifurcation with symmetries, on Hopf point continuation, and on branch switching from periodic orbits (periodic orbit pitchfork and period doubling bifurcations).

MSC: 35J47, 35B22, 37M20

Keywords: Hopf bifurcation, periodic orbit continuation, Floquet multipliers, partial differential equations, finite element method, reaction–diffusion, distributed optimal control

Contents

1	Introduction	2
2	Hopf bifurcation and periodic orbit continuation in <code>pde2path</code>	4
2.1	Branch and Hopf point detection and localization	5
2.2	Branch switching	8
2.3	The continuation of branches of periodic orbits	8
2.3.1	General setting	8
2.3.2	Arclength parametrization	9
2.3.3	Natural parametrization	11
2.4	Floquet multipliers	12
3	Four examples	14
3.1	A complex Ginzburg–Landau equation	14
3.2	Spiral waves on a disk	18
3.2.1	Bifurcations to rotating and standing waves	19
3.2.2	Spiral waves	21
3.3	An extended Brusselator	22
3.4	A canonical system from optimal control	26
4	Summary and outlook	30

1 Introduction

The package `pde2path` [UWR14, DRUW14, Uec18b] has originally been developed as a continuation/bifurcation package for stationary problems of the form

$$G(u, \lambda) := -\nabla \cdot (c \otimes \nabla u) + au - b \otimes \nabla u - f = 0. \quad (1)$$

Here $u = u(x) \in \mathbb{R}^N$, $x \in \Omega$ with $\Omega \subset \mathbb{R}^d$ some bounded domain, $d = 1, 2, 3$, $\lambda \in \mathbb{R}^p$ is a parameter (vector), and the diffusion, advection and linear tensors c, b, a , and the nonlinearity f , can depend on $x, u, \nabla u$, and parameters.¹ The boundary conditions (BC) are of “generalized Neumann” form

$$\mathbf{n} \cdot (c \otimes \nabla u) + qu = g, \quad (2)$$

where \mathbf{n} is the outer normal and again $q \in \mathbb{R}^{N \times N}$ and $g \in \mathbb{R}^N$ may depend on $x, u, \nabla u$ and parameters. These BC include zero flux BC, and a “stiff spring” approximation of Dirichlet BC via large prefactors in q and g , and periodic BC are also supported over suitable domains. Moreover, there are interfaces to couple (1) with additional equations, such as mass conservation, or phase conditions for considering co-moving frames, and to set up extended systems, for instance for fold point and branch point localization and continuation.

`pde2path` has been applied to various research problems, e.g., patterns in 2D reaction diffusion systems [UW14, Küh15b, Küh15a, SDE⁺15, Wet16, ZUFM17], some problems in fluid dynamics and nonlinear optics [ZHKR15, DU16, EWGT17] and in optimal control [Uec16, GU17]. Here we report on features and algorithms in `pde2path` to treat Hopf (or Poincaré–Andronov–Hopf) bifurcations and the continuation of time–periodic orbits for systems of the form

$$\partial_t u = -G(u, \lambda), \quad u = u(x, t), \quad x \in \Omega \subset \mathbb{R}^d, \quad d = 1, 2, 3, \quad t \in \mathbb{R} \quad (d + 1 \text{ dimensional problem}), \quad (3)$$

with G from (1) and BC from (2). Adding the time dimension makes computations more expensive, such that here we focus on 1D and 2D, and only give one 3D example to illustrate that all user interfaces are essentially dimension independent.

For general introductions to and reviews of (numerical) continuation and bifurcation we recommend [Gov00, Kuz04, Doe07, Sey10], and [Mei00], which has a focus on reaction–diffusion systems. The treatment of large scale problems, typically from the spatial discretization of PDEs, including the continuation of time periodic orbits, has for instance been discussed in [LRSC98, TB00, LR00, SNGAS04, SN10], and has recently been reviewed in [DWC⁺14, NS15, SN16]. There, the focus has been on matrix–free methods where the periodic orbits are computed by a shooting method, which can conveniently be implemented if a time–stepper for the given problem is available. In many cases, shooting methods can also be used to investigate the bifurcations from periodic orbits, and to trace bifurcation curves in parameter space, by computing the Floquet multipliers of the periodic orbits. In this direction, see in particular [SGN13, WIJ13, NS15, LRTT16] for impressive results in fluid problems.

Here we proceed by a collocation (in time) method for the continuation of periodic orbits. With respect to computation time and in particular memory requirements such methods are often more demanding than (matrix free) shooting methods. However, one reason for the efficiency of shooting

¹Originally, `pde2path` was based on the `Matlab pdetoolbox`, with $d = 2$. Then, as also detailed in the `pdetoolbox` documentation, $c \in \mathbb{R}^{N \times N \times 2 \times 2}$, $[\nabla \cdot (c \otimes \nabla u)]_i := \sum_{j=1}^N [\partial_x c_{ij11} \partial_x + \partial_x c_{ij12} \partial_y + \partial_y c_{ij21} \partial_x + \partial_y c_{ij22} \partial_y] u_j$ (i^{th} component), and similarly $b \in \mathbb{R}^{N \times N \times 2}$, $a \in \mathbb{R}^{N \times N}$ with $[b \otimes \nabla u]_i := \sum_{j=1}^N [b_{ij1} \partial_x + b_{ij2} \partial_y] u_j$, $[au]_i = \sum_{j=1}^N a_{ij} u_j$, and $f = (f_1, \dots, f_N)$ as a column vector. For $d = 1$ these formulas simplify drastically, while for $d = 3$ we refer to the `OOPDE` documentation. For a given PDE, there is some freedom how to distribute terms to a, b and f ; we typically set $a = 0$ in the genuine PDE implementation, and only use $a \neq 0$ for assembling linearizations. Altogether we recommend the tutorials and various demo directories included with `pde2path` [Uec18b] for hints how to implement a PDE of the form (1) (or (3)) in `pde2path`.

methods in the works cited above is that the problems considered there are strongly dissipative, with only few eigenvalues of the linearized evolution near the imaginary axis. We also treat such problems, and show that up to moderately large scale they can efficiently be treated by collocation methods as well. However, another class of problems we deal with are canonical systems obtained from distributed optimal control with infinite time horizon. Such problems are ill-posed as initial value problems, which seems quite problematic for genuine shooting methods.

We also compute the Floquet multipliers for periodic orbits. For this, a direct approach is to explicitly construct the monodromy matrix from the Jacobian used in the collocation solver for the periodic orbit. We find that this works well for dissipative problems, but completely fails for the ill-posed optimal control problems, and thus we also provide a method based on a periodic Schur decomposition, which can handle this situation.

To illustrate the performance of our `hopf` library we consider four example problems, with the `Matlab` files included as demo directories in the package download at [Uec18b], where also the `pde2path` user-guide [dWDR⁺18] with installation instruction, the tutorial [Uec18a] on Hopf bifurcations, and various other tutorials on how to run `pde2path` are available. The first example is a cubic–quintic complex Ginzburg–Landau (cGL) equation, which we consider over 1D, 2D, and 3D cuboids with homogeneous Neumann and Dirichlet BC, such that we can explicitly calculate all Hopf bifurcation points (HBP) from the trivial branch. For periodic BC we also have the Hopf branches explicitly, which altogether makes the cGL equation a nice toy problem to validate and benchmark our routines. Next we consider a reaction diffusion system from [GKS00] on a circular domain with Robin BC, which lead to the bifurcation of (standing and) rotating waves, and in particular of spiral waves, from the trivial solution branch. Our third example is a Brusselator system from [YDZE02], which shows interesting interactions between Turing branches and Turing–Hopf branches. As a non-dissipative example we treat the canonical system for a simple control problem of “optimal pollution”. This is still of the form (3), but is ill-posed as an initial value problem, since it includes “backward diffusion”. Nevertheless, we continue steady states, and obtain Hopf bifurcations and branches of periodic orbits.

Highly developed software packages for numerical continuation and bifurcation include `AUTO` [DCF⁺97], `CONTENT` [KLS96], and `MATCONT` [DGK03]. These mainly focus on algebraic equations and ordinary differential equations, but can also be used for PDEs, especially in 1D. See also `CL_MATCONT` [DGK⁺08], which has a focus on invariant subspace continuation that makes it suitable for larger scale computations [BFG⁺14], or `coco` [DS13] which is a general toolbox, which for instance has been coupled with `COMSOL` for a PDE problem in [FALD12], and `LOCA` [Sal16] or `oomphlib` [HH17] for continuation and bifurcation tools (libraries) aimed at PDEs. On the other hand, many of the numerical results on periodic orbits in PDEs in the literature, again see [DWC⁺14, NS15] for reviews, are based on custom made codes, which sometimes do not seem easy to access and modify for non-expert users. Although in some of our research applications we consider problems with on the order of 10^5 unknowns in space (and the largest Hopf demo here has 120000 total unknowns), `pde2path` is not primarily intended for very large scale problems. The goal of `pde2path` is to provide a general and easy to use (and modify and extend) toolbox to investigate bifurcations in PDEs of the (rather large) class given by (3). With the `hopf` library we provide some basic functionality for Hopf bifurcations and continuation of periodic orbits for such PDEs over 1D, 2D, and 3D domains, where at least the 1D cases and simple 2D cases are sufficiently fast to use `pde2path` as a quick (i.e., interactive) tool for studying interesting problems. The algorithms used for the Hopf problems, except maybe for the (heuristic) Hopf point detection in §2.1, are essentially taken from the literature, and our objective has been their user friendly implementation and seamless link with the `pde2path` structure. The user interfaces reuse the standard `pde2path` setup, and no new user functions are necessary. The results given here are for the same meshes as in the tutorial [Uec18a], which gives implementation details for these and some

more demos. Due to higher computational costs in 2+1D, in 3D, or even 3+1D, compared to the 2D case from [UWR14], in these demos we work with rather coarse meshes to quickly get familiar with the software. We checked for all examples that (spatially and temporally) finer meshes give consistent (i.e., qualitatively the same, and also quantitatively close) results, and in [Uec18a] give a number of comments on how to adaptively generate and work with finer meshes, but we refrain from a genuine convergence analysis.

In §2 we review some basics of the Hopf bifurcation, of periodic orbit continuation and multiplier computations, and explain their numerical treatment in `pde2path`. In §3 we present the demos, and §4 contains a brief summary and outlook. For comments, questions, and bugs, please mail to `hannes.uecker@uni-oldenburg.de`.

Acknowledgment. Many thanks to Francesca Mazzia for providing TOM [MT04], which was essential help for setting up the `hopf` library; to Uwe Prüfert for providing `OOPDE`; to Tomas Dohnal, Jens Rademacher and Daniel Wetzel for some testing of the Hopf examples; to Daniel Kressner for `pqzschur`; to Arnd Scheel for helpful comments on the system in §3.2; and to Dieter Grass for the cooperation on distributed optimal control problems, which was an important motivation to implement the `hopf` library. Additionally I want to thank three anonymous reviewers for invaluable comments on an earlier version of this paper.

2 Hopf bifurcation and periodic orbit continuation in `pde2path`

Our description of the algorithms is based on the spatial FEM discretization of (3), which, with a slight abuse of notation, we write as

$$M\dot{u}(t) = -G(u(t), \lambda), \quad (4)$$

where $M \in \mathbb{R}^{n_u \times n_u}$ is the mass matrix, $n_u = Nn_p$ is the number of unknowns (degrees of freedom DoF) with n_p is the number of mesh-points, and, for each t ,

$$u(t) = (u_{1,1}, \dots, u_{1,n_p}, u_{2,1}, \dots, u_{N,1}, \dots, u_{N,n_p})(t) \in \mathbb{R}^{n_u},$$

and similarly $G : \mathbb{R}^{n_u} \times \mathbb{R}^p \rightarrow \mathbb{R}^{n_u}$. We use the generic name λ for the parameter vector, *and* the *active* continuation parameter, again see [DRUW14] for details. Given a stationary solution u of (4), when in the following we discuss eigenvalues μ and eigenvectors ϕ of the linearization

$$M\dot{v} = -\partial_u G(u, \lambda)v \quad (5)$$

of (4) around u , or simply eigenvalues of $\partial_u G = \partial_u G(u, \lambda)$, we always mean the eigenvalue problem

$$\mu M\phi = \partial_u G\phi. \quad (6)$$

Thus eigenvalues of $\partial_u G$ with *negative* real parts give dynamical *instability* of u .

Remark 2.1. For, e.g., the continuation of traveling waves in translationally invariant problems, the PDE (3) is typically transformed to a moving frame $\xi = x - \gamma(t)$, with BC that respect the translational invariance, and where $\dot{\gamma}$ is an unknown wave speed, which yields an additional term $\dot{\gamma}\partial_x u$ on the rhs of (3). The reliable continuation of traveling waves then also requires a phase condition, i.e., an additional equation, for instance of the form $q(u) = \langle \partial_x \tilde{u}, u \rangle \stackrel{!}{=} 0$, where \tilde{u} is a reference wave (e.g. $\tilde{u} = u_{\text{old}}$, where u_{old} is from a previous continuation step), and $\langle u, v \rangle = \int_{\Omega} uv \, dx$. Together we obtain a differential–algebraic system instead of (4), and similarly for other constraints such as mass conservation, see [DRUW14, §2.4, §2.5] for examples, and for instance [BT07, RU17]

for equations with continuous symmetries and the associated “freezing method”. Hopf bifurcations can occur in such systems, see e.g. the Hopf bifurcations from traveling ($\dot{\gamma} \neq 0$) or standing ($\dot{\gamma} = 0$) fronts and pulses in [HM94, GAP06, BT07, GF13], but are somewhat more elaborate to treat numerically than the case without constraints. Thus, here we restrict to problems of the form (3) without constraints, and hence to (4) on the spatially discretized level, and refer to [RU17, Uec18a] for examples of Hopf bifurcations with constraints in `pde2path`. For instance, in [RU17, §4] we consider Hopf bifurcations to modulated traveling waves in a model for autocatalysis, and the Hopf bifurcation of standing breathers in a FitzHugh–Nagumo system, and in [Uec18a, §5] the Hopf bifurcation of modulated standing and traveling waves in the Kuramoto–Sivashinky equation with periodic boundary conditions.]

2.1 Branch and Hopf point detection and localization

Hopf bifurcation means the bifurcation of a branch of time periodic orbits from a branch $\lambda \mapsto u(\cdot, \lambda)$ of stationary solutions of (3), or numerically (4). This generically occurs if at some $\lambda = \lambda_H$ a pair of simple complex conjugate eigenvalues $\mu_j(\lambda) = \bar{\mu}_{j+1}(\lambda)$ of $G_u = \partial_u G(u, \lambda)$ crosses the imaginary axis with nonzero imaginary part and nonzero speed, i.e.,

$$\mu_j(\lambda_H) = \bar{\mu}_j(\lambda_H) = i\omega \neq 0, \quad \text{and } \text{Re}\mu'_j(\lambda_H) \neq 0. \quad (7)$$

Thus, the first issue is to define a suitable function ψ_H to numerically detect (7). Additionally, we also want to detect real eigenvalues crossing the imaginary axis, i.e.,

$$\mu_j(\lambda_{\text{BP}}) = 0, \quad \text{and } \text{Re}\mu'_j(\lambda_{\text{BP}}) \neq 0. \quad (8)$$

A fast and simple method for (8) is to monitor sign changes of the product

$$\psi(\lambda) = \prod_{i=1, \dots, n_u} \mu_i(\lambda) = \det(G_u) \quad (9)$$

of all eigenvalues, which even for large n_u can be done quickly via the LU factorization of G_u , respectively the extended matrix in arclength continuation, see [UWR14, §2.1]. This so far has been the standard setting in `pde2path`, but the drawback of (9) is that the sign of ψ only changes if an odd number of real eigenvalues crosses 0.

Unfortunately, there is no general method for (7) which can be used for large n_u . For small systems, one option would be

$$\psi_H(\lambda) = \prod_i (\mu_i(\lambda) + \mu_{i+1}(\lambda)), \quad (10)$$

where we assume the eigenvalues to be sorted by their real parts. However, this, unlike (9) requires the actual computation of all eigenvalues, which is not feasible for large n_u . Another option are dyadic products, [Kuz04, Chapter 10], which again is not feasible for large n_u .

If, on the other hand, (3) is a dissipative problem, then we may try to just compute n_{eig} eigenvalues of G_u of smallest modulus, which, for moderate n_{eig} can be done efficiently, and to count the number of these eigenvalues which are in the left complex half plane, and from this detect both (7) and (8).² The main issue then is to choose n_{eig} , which unfortunately is highly problem dependent, and for a given problem may need to be chosen large again.

Here we use the idea of computing only a few eigenvalues near suitable spectral shifts $i\omega_{1,2,\dots}$. To estimate the shifts, we use ideas from [GS96] and consider the function $g(z) = c^T(G_u - zM)^{-1}b$,

²To distinguish steady bifurcation points from fold points, we then additionally need to check that $G_\lambda \notin R(G_\lambda)$.

which is the Schur complement of the bordered extension $\begin{pmatrix} G_u - zM & b \\ c^T & 0 \end{pmatrix}$ with (some choices of) $b, c \in \mathbb{R}^{n_u}$. By Cramer's rule we have

$$g(z) = \frac{N(z)}{\det(G_u - zM)}, \quad (11)$$

where N is a polynomial in z which depends on b, c . Thus, a geometrically simple eigenvalue μ of G_u (in the sense (6)) is a pole of g , if b is not in the range of $G_u - \mu M$ and if c is not orthogonal to the null space of $G_u - \mu M$. Expanding this idea, it is shown in [GS96] that if no pole or zero of g has real part zero, then

$$W(g(i\omega), 0, \infty) = \frac{\pi}{2}(Z_l - Z_r + P_r - P_l), \quad (12)$$

where $W(g(i\omega), 0, \infty)$ is the winding number of g , and $Z_{l,r}, P_{l,r}$ are the zeros and poles of $g(z)$ in the left and right complex half planes, respectively.

Here we only use the idea that for *generic choices* of b , and $c = b$, $g(i\omega)$ is large if $i\omega$ is close to an eigenvalue μ . The algorithm can be made more robust by choosing multiple b and using the max of $g(i\omega)$ over these b , but in practice just using

$$b = (1, 1, \dots, 1)/\sqrt{n_u} \quad (13)$$

works well. Thus, given a current solution (u, λ) we choose some ω_{\max} (either user defined, or $\omega_{\max} = \|G_u\|_1$) and compute the function

$$[0, \omega_{\max}] \ni \omega \mapsto g(u, \lambda, i\omega; b) := b^T (G_u - i\omega)^{-1} b, \quad (14)$$

with b from (13), and take (one or several) maxima of this function as shifts ω_j during the next continuation steps.³ I.e., after each continuation step we compute a few eigenvalues near $0, i\omega_1, \dots$ and check their real parts. We can reset the shifts ω_i after a number of continuation steps by evaluating (14) again, and instead of using (14) the user can also set the ω_i by hand.⁴

Of course, the idea is mainly heuristic, and in this simple form may miss some bifurcation points (BPs, in the sense of (8)) and Hopf bifurcation points (HBPs, in the sense of (7)), and can and typically will detect false BPs and HBPs, see Fig. 1, which illustrates two ways in which the algorithm can fail.⁵ However, some of these failures can be detected and/or corrected, see Remark 2.2, and in practice we found the algorithm to work remarkably well in our examples, with a rather small numbers of eigenvalues computed near 0 and $i\omega_1$, and in general to be more robust than the theoretically more sound usage of (12).⁶ For convenience, in the following we refer to these algorithms as

³To accurately compute g from (14) we use ideas from [GS96] to refine the ω discretization (and actually compute the winding number). The `pde2path` function `initeig` computes and plots $|g|$ (see Fig. 9(c) for an example), and this plot should be inspected for assurance that ω_{\max} has been chosen large enough.

⁴In principle, instead of using (14) we could also compute the guesses ω_i by computing eigenvalues of $G_u(u, \lambda)$ at a given (u, λ) ; however, this may itself either require a priori information on the pertinent ω_i (for shifting), or we may again need to compute a large number of eigenvalues of G_u . Thus we find (14) more simple, efficient and elegant.

⁵A third typical kind of failure is that during a continuation step a number m of eigenvalues crosses the imaginary axis close to $i\omega_1$, and simultaneously m already unstable eigenvalues leave the pertinent circle to the left due to a decreasing real part. The only remedy for this is to decrease the step-length ds . Clearly, a too large ds can miss bifurcations even if we could compute *all* eigenvalues, for instance if along the true branch eigenvalues cross back and forth.

⁶However, if additionally to bifurcations one is interested in the stability of (stationary) solutions, then the numbers of eigenvalues should not be chosen too small; otherwise the situation in Fig. 1(c,d) may easily occur, i.e., undetected eigenvalues with negative real parts.

- HD1** (Hopf Detection 1) compute the n_{eig} smallest eigenvalues of $\partial_u G$ and count those with negative real parts;
- HD2** (Hopf Detection 2) initially compute a number of guesses ω_j , $j = 1, \dots, g$ for spectral shifts, then compute the $n_{\text{eig},j}$ eigenvalues of $\partial_u G$ closest to $i\omega_j$, and count how many have negative real parts to detect crossings of eigenvalues near $i\omega_j$. Update the shifts when appropriate.

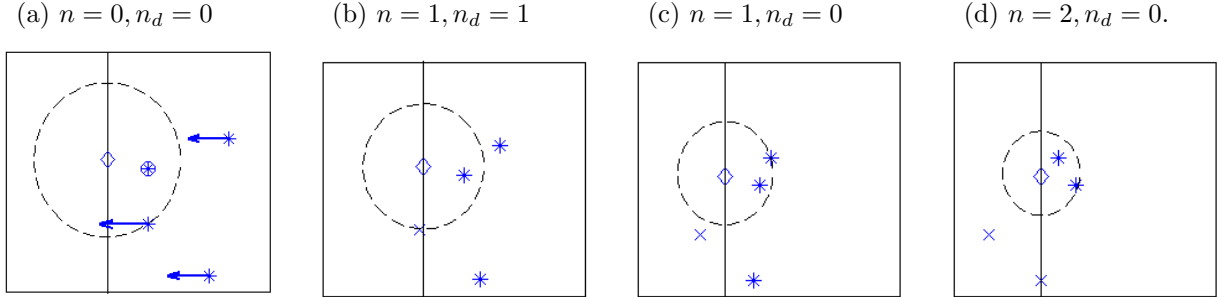


Figure 1: Sketch of the idea, and typical failures, of detecting Hopf points by counting eigenvalues with negative real parts near some shift $i\omega_1$, marked by \diamond , which can be somewhere between 0 and $\omega_{\max}/2$, say, with ω_{\max} suitably chosen, see footnote 3. Here, for illustration we use $n_{\text{eig}}=2$, i.e., use the 2 eigenvalues closest to $i\omega_1$ for bifurcation detection, and show 4 eigenvalues near $i\omega_1$, stable ones with $*$ and unstable ones with \times . n is the total number of negative eigenvalues, and n_d the number of detected ones. From (a) to (d) we assume that some parameter λ varies, and the shown eigenvalues depend continuously on λ ; for better illustration we assume that the eigenvalue circled in (a) stays fixed. The dashed circle has radius $|\mu(\lambda) - i\omega_1|$ with μ the second closest eigenvalue to $i\omega_1$. From (a) to (b) we correctly detect a HBP. From (b) to (c) we incorrectly find a HBP, as the only unstable eigenvalue wanders out of the pertinent circle. From (c) to (d) we miss a HBP, as the guess $i\omega_1$ is too far off. The failure (b) to (c) can be detected in the localization by requiring that at the end the real part of the eigenvalue closest to the imaginary axis is sufficiently small. The failure from (c) to (d) can be resolved by either (i) computing more eigenvalues close to $i\omega_1$, or (ii) by updating $i\omega_1$ using (14).

After detection of a (possible) BP or a (possible) HBP, or of several of these along a branch between s_0 and $s_0 + ds$, it remains to locate the BP or HBP. Again, there are various methods to do this, using, e.g., suitably extended systems [Gov00]. However, so far we typically use a simple bisection, which works well and sufficiently fast in our examples.⁷

Remark 2.2. To avoid unnecessary bisections and false BPs and HBPs we proceed as follows. After detection of a BP or HBP *candidate* with shift $i\omega_j$, we check if the eigenvalue μ closest to $i\omega_j$ has $|\text{Re}\mu| \leq \mu_1$, with default $\mu_1 = 0.01$. If not, then we assume that this was a false alarm. Similarly, *after completing* a bisection we check if the eigenvalue μ then closest to $i\omega_j$ has $|\text{Re}\mu| < \mu_2$, with default $\mu_2 = 0.0001$, and only then accept the computed point as a BP (if $\omega_j = 0$) or HBP (if $\omega_j > 0$). In our examples, about 50% of the candidates enter the bisection, and of these about 10% are rejected afterwards, and no false BPs or HBPs are saved to disk. This seems to be a reasonable compromise between speed and not missing BPs and HBPs and avoiding false ones. However, the values of μ_1, μ_2 are of course highly problem dependent. For instance, if the problem is strongly dissipative with a rather large spacing of the real parts of the eigenvalues, then it may be needed and efficient to increase μ_1 , and possibly μ_2 .]

⁷The only extended systems we deal with in `pde2path` so far are those for localization and continuation of stationary branch points, and of fold points, see [DRUW14, §2.1.4] or [UW17].

2.2 Branch switching

Branch switching at a (simple, see Remark 2.3 below) BP works as usual by computing an initial guess from the normal form of the stationary bifurcation, see [UWR14, §2.1]. Similarly, to switch to a Hopf branch of time periodic solutions we compute an initial guess from an approximation of the normal form

$$\dot{w} = \mu(\lambda)w + c_1(\lambda)|w|^2w, \quad (15)$$

of the bifurcation equation on the center manifold associated to $(\lambda, \mu) = (\lambda_H, i\omega_H)$. Thus we use

$$\mu(\lambda) = \mu_r(\lambda) + i\mu_i(\lambda) = \mu'_r(\lambda_H)(\lambda - \lambda_H) + i(\omega_H + \mathcal{O}(\lambda - \lambda_H)) + \mathcal{O}((\lambda - \lambda_H)^2), \quad (16)$$

and with $w = re^{i\omega_H t}$ replace (15) by

$$0 = r \left[\mu'_r(\lambda_H)(\lambda - \lambda_H) + c_1(\lambda_H)|r|^2 \right]. \quad (17)$$

Following [Kuz04], $c_1 = c_1(\lambda_H) \in \mathbb{R}$ is related to the first Lyapunov coefficient l_1 by $c_1(\lambda_H) = \omega_H l_1$, and we use the formulas from [Kuz04, p531-536] for the numerical computation of l_1 . Setting $\lambda = s\varepsilon^2$ with $s = \pm 1$ we then have a nontrivial solution

$$r = \varepsilon\alpha, \quad \alpha = \sqrt{-s\mu'(\lambda_H)/c_1(\lambda_H)} \quad (18)$$

of (17) for $s = -\text{sign}(\mu'(\lambda_H)/c_1)$, and thus take

$$\lambda = \lambda_H + s\varepsilon^2, \quad u(t) = u_0 + 2\varepsilon\alpha \text{Re}(e^{-i\omega_H t}\Psi), \quad (19)$$

as an initial guess for a periodic solution of (4) with period near $2\pi/\omega$. The approximation (19) of the bifurcating solution in the center eigenspace, also called linear predictor, is usually accurate enough, and is the standard setting in the `pde2path` function `hoswibra`, see [Uec18a]. The coefficients $s = \pm 1$ and α in (19) are computed, and ε is then chosen in such a way that the initial step length is `ds` in the norm (23) below.

Remark 2.3. Although multiple branch points, which naturally occur if the system has some symmetries, are not yet officially supported in `pde2path`, we have some preliminary routines for multiple steady bifurcations which we hope to include in the next version of `pde2path`. Similarly, (19) is only for simple Hopf points. This holds for all examples considered below, except for the patterns on a disk in §3.2, where we give further remarks on a double Hopf case.]

2.3 The continuation of branches of periodic orbits

2.3.1 General setting

The continuation of the Hopf branch is, as usual, a predictor–corrector method, and for the corrector we offer, essentially, two different methods, namely natural and arclength continuation. For both, we reuse the standard `pde2path` settings for assembling G in (3) and Jacobians, such that the user does not have to provide new functions. In any case, first we rescale $t = Tt$ in (4) to obtain

$$M\dot{u} = -TG(u, \lambda), \quad u(\cdot, 0) = u(\cdot, 1), \quad (20)$$

with unknown period T , but with initial guess $T = 2\pi/\omega$ at bifurcation.

2.3.2 Arclength parametrization

We start with the arclength setting, which is more general and more robust, although the continuation in natural parametrization in `pde2path` has other advantages such as error control and adaptive mesh refinement for the time discretization, built into TOM, which we have not yet implemented in the arclength setting. We use the phase condition

$$\phi := \int_0^1 \langle u(t), \dot{u}_0(t) \rangle dt \stackrel{!}{=} 0, \quad (21)$$

where $\langle \cdot, \cdot \rangle$ is the scalar product in \mathbb{R}^{n_u} and $\dot{u}_0(t)$ is from the previous continuation step, and we use the step length condition

$$\psi := \xi_H \sum_{j=1}^m \langle u(t_j) - u_0(t_j), u'_0(t_j) \rangle + (1 - \xi_H) [w_T(T - T_0)T'_0 + (1 - w_T)(\lambda - \lambda_0)\lambda'_0] - ds \stackrel{!}{=} 0, \quad (22)$$

where again T_0, λ_0 are from the previous step, ds is the step-length, $' = \frac{d}{ds}$ denotes differentiation with respect to arclength, ξ_H and w_T denote weights for the u and T components of the unknown solution, and $t_0 = 0 < t_1 < \dots < t_m = 1$ is the temporal discretization. Thus, the step length is ds in the weighted norm

$$\|(u, T, \lambda)\|_{\xi} = \sqrt{\xi_H \left(\sum_{j=1}^m \|u(t_j)\|_2^2 \right) + (1 - \xi_H) [w_T T^2 + (1 - w_T) \lambda^2]}. \quad (23)$$

Even if ξ_H is similar to the (average) mesh-width in t , then the term $\xi_H \sum_j \|u(t_j)\|_2^2$ is only a crude approximation of the “natural length” $\int_0^1 \|u(t)\|_2^2 dt$. However, the choice of the norm is somewhat arbitrary, and we found (23) most convenient. Typically we choose $w_T = 1/2$ such that T and λ have the same weight in the arclength. A possible choice for ξ_H to weight the mn_u components of u is $\xi_H = \frac{1}{mn_u}$. However, in practice we choose

$$\xi_H = \frac{10}{mn_u}, \quad (24)$$

since at the Hopf bifurcation the branches are “vertical” ($\|u - u_0\| = \mathcal{O}(\sqrt{|\lambda - \lambda_0|})$, cf. (19)), and ξ_H tunes the search direction in the extended Newton loop between “horizontal” (large ξ_H) and “vertical” (small ξ_H). This could also be fine tuned by using α from (18), i.e., increase ξ_H further for large α , but (24) seems quite robust. See also [UWR14, §2.1] for the analogous role of ξ for stationary problems.

The integral in (21) is discretized as a simple Riemann sum, such that the derivative of ϕ with respect to u is, with $\tilde{u}_0(t) = \dot{u}_0(t)$,

$$\partial_u \phi = (h_1 \tilde{u}(t_1)_1, \dots, h_1 \tilde{u}(t_1)_{n_u}, h_2 \tilde{u}(t_2)_1, \dots, h_2 \tilde{u}(t_2)_{n_u}, \dots, h_{l-1} \tilde{u}(t_{m-1})_{n_u}, 0, \dots, 0), \quad (25)$$

n_u zeros at the end, where $h_l = t_{l+1} - t_l$ is the mesh-size in the time discretization. Similarly, denoting the tangent along the branch as

$$\tau = (\tau_u, \tau_T, \tau_\lambda), \quad \tau_u \in \mathbb{R}^{1 \times mn_u} \text{ (row vector as in (25))}, \quad \tau_T, \tau_\lambda \in \mathbb{R}, \quad (26)$$

we can rewrite ψ in (22) as

$$\psi = \xi_H \tau_u (u - u_0) + (1 - \xi_H) (w_T \tau_T (T - T_0) + (1 - w_T) \tau_\lambda (\lambda - \lambda_0)) - ds. \quad (27)$$

Setting $U = (u, T, \lambda)$, and writing (20) as $\mathcal{G}(u, T, \lambda) = 0$, in each continuation step we thus need to solve

$$H(U) := \begin{pmatrix} \mathcal{G}(U) \\ \phi(u) \\ \psi(U) \end{pmatrix} \stackrel{!}{=} \begin{pmatrix} 0 \\ 0 \\ 0 \end{pmatrix} \in \mathbb{R}^{mn_u+2}, \quad (28)$$

for which we use Newton's method, i.e.,

$$U^{j+1} = U^j - \mathcal{A}(U^j)^{-1} H(U^j), \quad \mathcal{A} = \begin{pmatrix} \partial_u \mathcal{G} & \partial_T \mathcal{G} & \partial_\lambda \mathcal{G} \\ \partial_u \phi & 0 & 0 \\ \xi_H \tau_u & (1 - \xi_H) w_T \tau_T & (1 - \xi_H)(1 - w_T) \tau_\lambda \end{pmatrix}. \quad (29)$$

After convergence of U^j to U , i.e., $\|H(U)\| \leq \text{"tolerance"}$ in some suitable norm, the next tangent τ_1 with preserved orientation $\langle \tau_0, \tau_1 \rangle > 0$ can be calculated as usual from

$$\mathcal{A}(U) \tau_1 = (0, 0, 1)^T. \quad (30)$$

It remains to discretize in time and assemble \mathcal{G} in (28) and the Jacobian $\partial_u \mathcal{G}$. For this we use (modifications of) routines from TOM [MT04], which assumes the unknowns in the form

$$u = (u_1, \dots, u_m) = (u(t_1), u(t_2), \dots, u(t_m)), \quad (m \text{ time slices}), \quad (31)$$

Then, using the first order finite differences TOM setting we have, for $j = 1, \dots, m-1$, the implicit backwards in time finite differences

$$(\mathcal{G}(u))_j = -h_{j-1}^{-1} M(u_j - u_{j-1}) - \frac{1}{2} T(G(u_j) + G(u_{j-1})), \quad (32)$$

where $u_0 := u_{m-1}$, and additionally the periodicity condition

$$G_m(u) = u_m - u_1. \quad (33)$$

The Jacobian is $\partial_u \mathcal{G} = A_1$, where we set, as it reappears below for the Floquet multipliers,

$$A_\gamma = \begin{pmatrix} M_1 & 0 & 0 & 0 & \dots & -H_1 & 0 \\ -H_2 & M_2 & 0 & 0 & \dots & 0 & 0 \\ 0 & -H_3 & M_3 & 0 & \dots & 0 & 0 \\ \vdots & \dots & \ddots & \ddots & \ddots & \vdots & \vdots \\ 0 & \dots & \dots & \ddots & \ddots & 0 & 0 \\ 0 & \dots & \dots & 0 & -H_{m-1} & M_{m-1} & 0 \\ -\gamma I & 0 & \dots & \dots & \dots & 0 & I \end{pmatrix}, \quad (34)$$

where $M_j = -h_{j-1}^{-1} M - \frac{1}{2} T G_u(u_j)$, $H_j = -h_{j-1}^{-1} M + \frac{1}{2} T G_u(u_{j-1})$, and I is the $n_u \times n_u$ identity matrix. The derivatives $\partial_T \mathcal{G}$, $\partial_\lambda \mathcal{G}$ in (29) are cheap from numerical differentiation.

Remark 2.4. An alternative to the finite differences (32) is orthogonal collocation with piecewise polynomials, for instance used in AUTO, where also the order can be chosen. The use of TOM was initially motivated by connecting orbit problems from optimal control, see [Uec16, GU17, Uec17], where TOMs automatic mesh-refinement in t can deal very efficiently with sharp initial transitions. Moreover, TOM has been easy to adapt to the mass matrix M on the left hand side of (20). It was thus natural to also use TOM for time periodic orbits. TOM also provides options to use higher order finite differences, but so far we only use (32).]

Remark 2.5. $\mathcal{A} \in \mathbb{R}^{(mn_u+2) \times (mn_u+2)}$ in (29), (30) consists of $A = A_1 = \mathcal{G}_u \in \mathbb{R}^{mn_u \times mn_u}$, which is large but sparse, and borders of widths 2, i.e., symbolically,

$$\mathcal{A} = \begin{pmatrix} A & B \\ C & D \end{pmatrix}, \text{ with large and sparse } A, \text{ with } C^T, B \in \mathbb{R}^{mn_u \times 2}, \text{ and } D \in \mathbb{R}^{2 \times 2}.$$

There are various methods to solve bordered systems of the form

$$\mathcal{A}x = b, \quad b = \begin{pmatrix} f \\ g \end{pmatrix}, \quad (35)$$

see, e.g., [Gov00]. Here we use the very simple scheme

$$V = A^{-1}B, x_1 = A^{-1}f, \tilde{D} = D - CV, y_1 = g - Cx_1, y_2 = \tilde{D}^{-1}y_1, x_2 = x_1 - Vy_2, x = \begin{pmatrix} x_2 \\ y_2 \end{pmatrix}. \quad (36)$$

The big advantage of such bordered schemes is that solving systems such as $Ax_1 = f$ (where we either pre-factor A for repeated solves, or use a preconditioned iterative method) is usually much cheaper due to the structure of A than solving $\mathcal{A}x = b$ (either by factoring \mathcal{A} , or by an iterative method with some preconditioning of \mathcal{A}).⁸

The scheme (36) may suffer from some instabilities, but often these can be corrected by a simple iteration: If $\|r\|$ with $r = \mathcal{A}x - b$ is too large, then we solve $\mathcal{A}\hat{x} = r$ (again by (36), which is cheap) and update $x = x - \hat{x}$, until $\|r\| \leq$ “tolerance”. We in particular sometimes obtain poor solutions of (35) for $b = (0, 0, 1)^T$ from (30), but they typically can be improved by a few iterations. Altogether we found the scheme (36) to work well in our problems, with a typical speedup of up to 50 compared to the direct solution of $\mathcal{A}x = b$. Again, see [Gov00] for alternative schemes and detailed discussion.

For the solutions of $AV = B$ and $Ax_1 = f$ in (36) we give the option to use a preconditioned iterative solver from `ilupack` [Bol11], see also [UW17].⁹ The number of continuation steps before a new preconditioner is needed can be quite large, and often the iterative solvers give a significant speedup.]

2.3.3 Natural parametrization

By keeping λ fixed during correction we cannot pass around folds, but on the other hand can take direct advantage of further important features of TOM. TOM requires separated boundary conditions, and thus we use a standard trick and introduce, in the notation (31), auxiliary variables $\tilde{u} = (\tilde{u}_1, \tilde{u}_2, \dots, \tilde{u}_m)$ and additional (dummy) ODEs $\dot{\tilde{u}} = 0$. Then setting the boundary conditions

$$u_1 - \tilde{u}_1 = 0, \quad u_m - \tilde{u}_m = 0 \quad (37)$$

corresponds via $u_m = \tilde{u}_m = \tilde{u}_1 = u_1$ to periodic boundary conditions for u . Moreover, we add the auxiliary equation $\dot{T} = 0$, and set up the phase condition

$$\phi = \langle u(0), \dot{u}_0(0) \rangle \stackrel{!}{=} 0 \quad (38)$$

⁸The special structure of A from (34) can also be exploited to solve $Ax = f$ in such a way that subsequently the Floquet multipliers can easily be computed, see §2.4, and [Lus01] for comments on the related algorithms used in AUTO.

⁹When using iterative solvers it is often advantageous to directly use them for the full system (35), since the preconditioners and iterative solvers seem rather indifferent to the borders.

as an additional boundary condition. Thus, the complete system to be solved is

$$\begin{pmatrix} M\dot{u} \\ \dot{\tilde{u}} \\ \dot{T} \end{pmatrix} = \begin{pmatrix} -TG(u) \\ 0 \\ 0 \end{pmatrix}, \quad (39)$$

together with (37) and (38). We may then pass an initial guess (from a predictor) at a new λ to TOM, and let TOM solve for (u, \tilde{u}) and T . The main advantage is that for this we can directly use the error control and adaptive mesh refinement for the temporal discretization built into TOM.¹⁰

2.4 Floquet multipliers

The (in)stability of – and possible bifurcations from – a periodic orbit u_H are analyzed via the Floquet multipliers γ . These are obtained from finding nontrivial solutions (v, γ) of the variational boundary value problem

$$M\dot{v}(t) = -T\partial_u G(u(t))v(t), \quad (40)$$

$$v(1) = \gamma v(0). \quad (41)$$

By translational invariance of (20), there always is the trivial multiplier $\gamma_1 = 1$. Equivalently, the multipliers γ are the eigenvalues of the monodromy matrix $\mathcal{M}(u_0) = \partial_u \Phi(u_0, T)$, where $\Phi(u_0, t)$ is the solution of the initial value problem (4) with $u(0) = u_0$ from u_H . Thus, $\mathcal{M}(u_0)$ depends on u_0 , but the multipliers γ do not. $\mathcal{M}(u_0)$ has the eigenvalues $1, \gamma_2, \dots, \gamma_{n_u}$, where $\gamma_2, \dots, \gamma_{n_u}$ are the multipliers of the Poincaré map $\Pi(\cdot; u_0)$, which maps a point \tilde{u}_0 in a hyperplane Σ through u_0 and transversal to u_H to its first return to Σ , see, e.g., [Kuz04, Theorem 1.6]. Therefore, a necessary condition for the bifurcation from a branch $\lambda \mapsto u_H(\cdot, \lambda)$ of periodic orbits is that at some $(u_H(\cdot, \lambda_0), \lambda_0)$, additional to the trivial multiplier $\gamma_1 = 1$ there is a second multiplier γ_2 (or a complex conjugate pair $\gamma_{2,3}$) with $|\gamma_2| = 1$, which generically leads to the following bifurcations (see, e.g., [Sey10, Chapter 7] or [Kuz04] for more details):

- (i) $\gamma_2 = 1$, yields a fold of the periodic orbit, or a transcritical or pitchfork bifurcation of periodic orbits.
- (ii) $\gamma_2 = -1$, yields a period-doubling bifurcation, i.e., the bifurcation of periodic orbits $\tilde{u}(\cdot; \lambda)$ with approximately double the period, $\tilde{u}(\tilde{T}; \lambda) = \tilde{u}(0; \lambda)$, $\tilde{T}(\lambda) \approx 2T(\lambda)$ for λ near λ_0 .
- (iii) $\gamma_{2,3} = e^{\pm i\vartheta}$, $\vartheta \neq 0, \pi$, yields a torus (or Naimark–Sacker) bifurcation, i.e., the bifurcation of periodic orbits $\tilde{u}(\cdot, \lambda)$ with two “periods” $T(\lambda)$ and $\tilde{T}(\lambda)$; if $T(\lambda)/\tilde{T}(\lambda) \notin \mathbb{Q}$, then $\mathbb{R} \ni t \mapsto \tilde{u}(t)$ is dense in certain tori.

Here we are first of all interested in the computation of the multipliers. Using the same discretization for v as for u , it follows that γ and $v = (v_1, \dots, v_m)$ have to satisfy the matrix eigenvalue problem

$$A_\gamma v = 0, \quad (42)$$

for some $\gamma \in \mathbb{C}$. From this special structure it follows that $\mathcal{M}(u_{j_0})$ can be obtained from certain products involving the M_j and the H_j , for instance

$$\mathcal{M}(u_{m-1}) = M_{m-1}^{-1} H_{m-1} \cdots M_1^{-1} H_1. \quad (43)$$

Thus, a simple way to compute the γ_j is to compute the product (43) and subsequently (a number of) the eigenvalues of $\mathcal{M}(u_{m-1})$. We call this **FA1** (Floquet Algorithm 1), and using

$$\text{err}_{\gamma_1} := |\gamma_1 - 1| \quad (44)$$

¹⁰For the arclength setting we do not yet provide adaptive mesh-refinement in t based on error estimates, but only provide some ad-hoc local in t mesh-refinement, see [Uec18a].

as a measure of accuracy we find that this works fast and accurately for our dissipative examples. Typically $\text{err}_{\gamma_1} < 10^{-10}$, although at larger amplitudes of u_H , and if there are large multipliers, this may go up to $\text{err}_{\gamma_1} \sim 10^{-8}$, which is the (default) tolerance we require for the computation of u_H itself. Thus, in the software we give a warning if err_{γ_1} exceeds a certain tolerance tol_{fl} . However, for the optimal control example in §3.4, where we naturally have multipliers γ_j with $|\gamma_j| > 10^{30}$ and larger¹¹, **FA1** completely fails to compute any meaningful multipliers.

More generally, in for instance [FJ91, Lus01] it is discussed that methods based directly on (43)

- may give considerable numerical errors, in particular if there are both, very small and very large multipliers γ_j ;
- discard much useful information, for instance eigenvectors of $\mathcal{M}(u_l)$, $l \neq m - 1$, which are useful for branch switching.

As an alternative, [Lus01] suggests to use a periodic Schur decomposition [BGVD92] to compute the multipliers (and subsequently pertinent eigenvectors), and gives examples that in certain cases this gives much better accuracy, according to (44). See also [Kre01, Kre06] for similar ideas and results.

We thus provide an algorithm **FA2** (Floquet Algorithm 2), which, based on `pqzscher` from [Kre01], computes a periodic Schur decomposition of the matrices involved in (43), from which we immediately obtain the multipliers, see Remark 2.6(d). For large n_u and m , **FA2** gets rather slow, and thus we rather use it in two ways. First, to validate (by example) **FA1**, and second to compute the multipliers when **FA1** fails, in particular for our OC example.

In summary, for small to medium sized *dissipative* problems, i.e., $n_u * m < 50000$, say, computing (a number of) multipliers with **FA1** is a matter of a seconds. For the *ill-posed* OC problems we have to use **FA2** which is slower and for medium sized problems can be as slow as the computation of u_H . In any case, for efficiency we also give the option to switch off the simultaneous computation of multipliers during continuation of periodic orbits.

Remark 2.6. (a) To save the stability information on the computed branch we define

$$\text{ind}(u_H) = \text{number of multipliers } \gamma \text{ with } |\gamma| > 1 \text{ (numerically: } |\gamma| > 1 + \text{tol}_{\text{fl}}), \quad (45)$$

such that unstable orbits are characterized by $\text{ind}(u_H) > 0$. Thus, a change in $\text{ind}(u_H)$ signals a possible bifurcation, and via

$$\gamma_{\text{cand}} := \text{argmin}\{|\gamma_j| - 1 : j > 1\}$$

we also get an approximation for the critical multiplier, and thus a classification of the possible bifurcation in the sense (i)-(iii).

(b) In **FA1** we compute n_+ multipliers $\gamma_2, \dots, \gamma_{n_+}$ of largest modulus (recall that we reserve γ_1 for the trivial multiplier), with $|\gamma_2| \geq |\gamma_3| \geq \dots \geq |\gamma_{n_+}|$, and count how many of these have $|\gamma_j| > 1$, which gives $\text{ind}(u_H)$ if we make sure that $|\gamma_{n_+}| < 1$. For dissipative systems, typically $0 \leq n_+ \ll n_u$, and the large multipliers of \mathcal{M} can be computed efficiently and reliably by vector iteration. However, it does happen that some of the small multipliers do not converge, in which case we also give a warning, and recommend to check the results with **FA2**.

(c) The idea of the periodic Schur decomposition is as follows. Given two collections $(A_i), (B_i)$, $i = 1, \dots, m$, of matrices $A_i, B_i \in \mathbb{C}^{n \times n}$, `pqzscher` computes $Q_i, Z_i, \tilde{A}_i, \tilde{B}_i \in \mathbb{C}^{n \times n}$ such that \tilde{A}_i, \tilde{B}_i are upper triangular, Q_i, Z_i are orthogonal, and

$$\begin{aligned} A_1 &= Q_1 \tilde{A}_1 Z_m^H, & B_1 &= Q_1 \tilde{B}_1 Z_1^H \\ A_2 &= Q_2 \tilde{A}_2 Z_1^H, & B_2 &= Q_2 \tilde{B}_2 Z_2^H \\ &\dots, & &\dots \\ A_m &= Q_m \tilde{A}_m Z_{m-1}^H, & B_m &= Q_m \tilde{B}_m Z_m^H. \end{aligned}$$

¹¹I.e., $|\gamma_{n_u}| \rightarrow \infty$ as $n_u \rightarrow \infty$, although the orbits may still be stable in the sense of optimal control, see §3.4

Consequently, for the product $\mathcal{M} = B_m^{-1}A_m \cdots B_1^{-1}A_1$ we have

$$\mathcal{M} = Z_m \tilde{B}_m^{-1} \tilde{A}_m \cdots \tilde{B}_1^{-1} \tilde{A}_1 Z_m^H,$$

and similar for products with other orderings of the factors. In particular, the eigenvalues of \mathcal{M} are given by the products $d_i = \prod_{j=1}^m \tilde{a}_{ii}^{(j)} / \tilde{b}_{ii}^{(j)}$, and, moreover, the associated eigenvectors can also be extracted from the Q_j, Z_j , see [Kre06] for further comments.

(d) Alternatively to using Floquet multipliers, we can assess the stability of the periodic orbits by using the time-integration routines from `pde2path`, which moreover has the advantage of giving information about the evolution of perturbations of unstable solutions; see §3 for examples, where in all cases perturbations of unstable periodic orbits lead to convergence to some other (stable) periodic orbit.]

3 Four examples

To illustrate the performance of our algorithms we use four examples, included as demos directories in the package download, together with the tutorial [Uec18a] explaining implementation details. Thus, here we focus on explaining the results (i.e., the relevant plots), and on relating them to some mathematical background of the equations. As already noted in the introduction, in these (tutorial) examples the meshes are chosen rather coarse, to quickly get familiar with the algorithms. In some problems we additionally switch off the simultaneous computation of Floquet multipliers, and instead compute the multipliers a posteriori at selected points on branches. Nevertheless, even with the coarse meshes some commands, e.g., the continuation of Hopf branches in 3+1D, may take several minutes. All computational times given in the following are from an i7 quad-core laptop with Linux Mint 18.1 and `Matlab` 2016b. Using the `ilupack` [Bol11] iterative linear solvers, memory requirements are moderate ($< 2\text{GB}$), but using direct solvers we need about 13GB for the largest scale problems considered here (3D cGL with about 120000 degrees of freedom).

3.1 A complex Ginzburg–Landau equation

We consider the cubic-quintic complex Ginzburg–Landau equation

$$\partial_t u = \Delta u + (r + i\nu)u - (c_3 + i\mu)|u|^2 u - c_5|u|^4 u, \quad u = u(t, x) \in \mathbb{C}, \quad (46)$$

with real parameters r, ν, c_3, μ, c_5 . Equations of this type are canonical models in physics, and are often derived as amplitude equations for more complicated pattern forming systems [AK02, Mie02]. Using real variables u_1, u_2 with $u = u_1 + iu_2$, (46) can be written as a real 2-component system of the form (3), i.e.,

$$\partial_t \begin{pmatrix} u_1 \\ u_2 \end{pmatrix} = \begin{pmatrix} \Delta + r & -\nu \\ \nu & \Delta + r \end{pmatrix} \begin{pmatrix} u_1 \\ u_2 \end{pmatrix} - (u_1^2 + u_2^2) \begin{pmatrix} c_3 u_1 - \mu u_2 \\ \mu u_1 + c_3 u_2 \end{pmatrix} - c_5 (u_1^2 + u_2^2)^2 \begin{pmatrix} u_1 \\ u_2 \end{pmatrix}. \quad (47)$$

We set

$$c_3 = -1, c_5 = 1, \nu = 1, \mu = 0.1, \quad (48)$$

and use r as the main bifurcation parameter. Considering (47) on boxes

$$\Omega = (-l_1\pi, l_1\pi) \times \cdots \times (-l_d\pi, l_d\pi) \quad (49)$$

with homogeneous Dirichlet BC or Neumann BC, or with periodic BC, we can explicitly calculate all Hopf bifurcation points from the trivial branch $u = 0$, and, for periodic BC, (some of) the bifurcating time periodic branches. For this consider the traveling wave ansatz

$$u(x, t) = ae^{i(\omega t - k \cdot x)}, \text{ with wave vector } k = (k_1, \dots, k_d), k_j \in \frac{1}{2l_j}\mathbb{Z}, \quad (50)$$

and temporal period $2\pi/\omega$, which yields

$$|a|^2 = |a(k, r)|^2 = -\frac{c_3}{2c_5} \pm \sqrt{\frac{c_3^2}{4c_5^2} + r - |k|^2}, \quad \omega = \omega(k, r) = \nu - \mu|a|^2, \quad |k|^2 = k_1^2 + \dots + k_d^2. \quad (51)$$

Note that ω and hence the period $T = 2\pi/\omega$ depend on $|a|$, that $u(x, t)$ on each branch is a single harmonic in x and t , and that the phase of a is free. Using (48) we obtain subcritical Hopf bifurcations of solutions (50) at

$$r = |k|^2, \text{ with folds at } r = |k|^2 - \frac{1}{4}. \quad (52)$$

Moreover, for these orbits we can also compute the Floquet multipliers explicitly. For instance, restricting to $k = 0$ in (50), and also to the invariant subspace of spatially independent perturbations, in polar-coordinates $\tilde{u}(t) = \tilde{a}(t)e^{i\tilde{\phi}(t)}$ we obtain the (here autonomous) linearized ODEs

$$\frac{d}{dt}\tilde{a} = h(r)\tilde{a}, \quad \frac{d}{dt}\tilde{\phi} = -2\mu a\tilde{a}, \text{ where } h(r) = r + 3a^2 - 5a^4. \quad (53)$$

The solution is $\tilde{a}(T) = e^{h(r)T}\tilde{a}(0)$, $\tilde{\phi}(T) = \tilde{\phi}(0) + \frac{a}{h(r)}(e^{h(r)T} - 1)\tilde{a}(0)$, and therefore the analytic monodromy matrix (in the $k=0$ subspace) is $\mathcal{M}_{k=0} = \begin{pmatrix} e^{h(r)T} & 0 \\ \frac{a}{h(r)}(e^{h(r)T} - 1) & 1 \end{pmatrix}$ with multipliers $\gamma_1=1$ and $\gamma_2=e^{h(r)T}$.

For periodic BC, the translational and reflection symmetry in x yield that the HBPs at $r=|k|^2>0$ have at least double multiplicity [Hoy06, GS02]. In for instance 1D, additional to the right traveling wave (50), left traveling waves bifurcate ($k \mapsto -k$), and it further follows (see also the comments after (59) for a related problem) that additional to the traveling waves, (families of) standing waves (SW) of the form $u(x, t) = b(t)\phi(x)$ with temporal period near $2\pi/\nu$ bifurcate, e.g.,

$$u(x, t) = b(t)(\cos(kx) + \text{higher harmonics in } x). \quad (54)$$

Boundary conditions that break the translational invariance, e.g., homogeneous Neumann or Dirichlet BC, then generically make the HBPs simple again and select the standing waves. Thus, (47) makes a nice toy problem to validate and benchmark our routines, where for simplicity we use Neumann and Dirichlet BC. For these we still have the formula $r = |k|^2$ for the HBPs, although we lose the explicit traveling wave branches.

There are no real eigenvalues of $\partial_u G$ on the trivial branch $u = 0$ in this example. Thus, for the HBP detection we can simply use algorithm **HD1** from page 7 and postpone to §3.3 and §3.4 the discussion of problems which require **HD2**. In 1D we use Neumann BC, and $n_x = 31$ spatial, and as the lowest temporal resolution (without mesh-refinement) $m = 20$ discretization points. For illustration we compute the first two bifurcating branches, **b1** and **b2**, using the arclength setting from the start, while for the third branch **b3** we first do 5 steps in natural parametrization, where TOM refines the starting t -mesh of 21 points to 41 points. This produces the plots in Fig. 2, where the norm in (a) is

$$\|u\|_* := \|u\|_{L^2(\Omega \times (0, T), \mathbb{R}^N)} / \sqrt{T|\Omega|}, \quad (55)$$

which is our default norm for Hopf branches. The simulations run in less than 10 seconds per branch, but the rather coarse meshes lead to some inaccuracies. For instance, the first three HBPs, which analytically are at $r = 0, 1/4, 1$, are obtained at $r = 6 * 10^{-5}, 0.2503, 1.0033$, and the period plot in (d) also shows some visible errors in the period T . However, these numerical errors quickly decay if we increase n_x and m , and runtimes stay small.

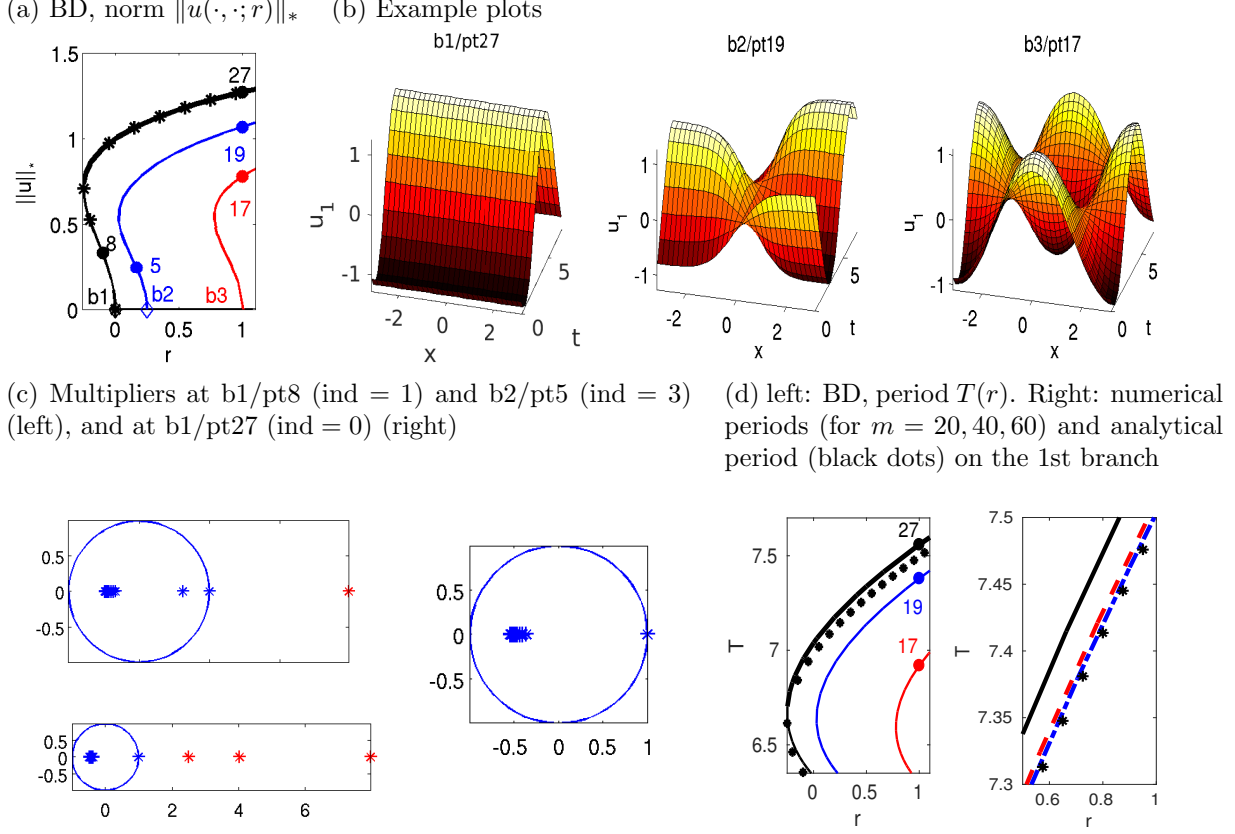


Figure 2: Numerical bifurcation diagrams (BD), example plots and (leading 20) Floquet multipliers for (47) on the domain $\Omega = (-\pi, \pi)$ with Neumann BC, 31 grid-points in x . Parameters $(\nu, \mu, c_3, c_5) = (1, 0.1, -1, 1)$, hence bifurcations at (restricting to the first three branches) $r = 0$ ($k = 0$, spatially homogeneous branch, black), $r = 1/4$ ($k = 1/2$, blue) and $r = 1$ ($k = 1$, red), see (52). The thick part of the black line in (a) indicates the only stable periodic solutions. The black dots in (a) and (d) are from the $k = 0$ analytical solution (51) (which also holds for Neumann BC in the $k = 0$ subspace). For $m = 20$ there is a visible error in T . The right panel of (d) shows the numerical T for different m ($m = 20$ black, $m = 40$ red-dashed, $m = 60$ blue-dotted), which illustrates the convergence of the numerical solution towards the analytical solution (51). Similarly, the periods also converge on the other branches.

On **b1**, initially there is one unstable multiplier γ_2 , i.e., $\text{ind}(u_H) = 1$, cf. (45), which passes through 1 to enter the unit circle at the fold. Its numerical value is 10^{-5} close to the analytical result from (53), and this error decreases upon refining the t -mesh. On **b2** we start with $\text{ind}(u_H) = 3$, and have $\text{ind}(u_H) = 2$ after the fold. Near $r = 0.45$ another multiplier moves through 1 into the unit circle, such that afterwards we have $\text{ind}(u_H) = 1$, with, for instance $\gamma_2 \approx 167$ at $r = 1$. Thus, we may expect a type (i) bifurcation (cf. p. 12) near $r = 0.45$, and similarly we can identify a number of possible bifurcation on **b3** and other branches. The trivial multiplier γ_1 is 10^{-12} close to 1 in all these computations, using **FA1**.

The basic 1D setup has to be modified only slightly for 2D and 3D. In 2D we choose homogeneous Dirichlet BC for u_1, u_2 . Then the first two HBPs are at $r_1 = 5/4$ ($k = (1/2, 1)$), and $r_2 = 2$

($k = (1, 1)$). Figure 3(a,b) shows some results obtained with $m = 20$ temporal points and a coarse mesh of 41×21 spatial points, hence $n_u = 1722$ spatial unknowns, yielding the numerical values $r_1 = 1.2526$ and $r_2 = 2.01$. Again, the numerical HBPs converge to the exact values when decreasing the mesh width, but at the prize of longer computations for the Hopf branches. Table 1 gives some timing and convergence indications in dependence of m , which in particular illustrates an advantage of the iterative solver for large total DoF. For the Floquet multipliers we obtain a similar picture as in 1D. The first branch has $\text{ind}(u_H) = 1$ up to the fold, and $\text{ind}(u_H) = 0$ afterwards, and on b2 $\text{ind}(u_H)$ decreases from 3 to 2 at the fold and to 1 near $r = 7.2$.

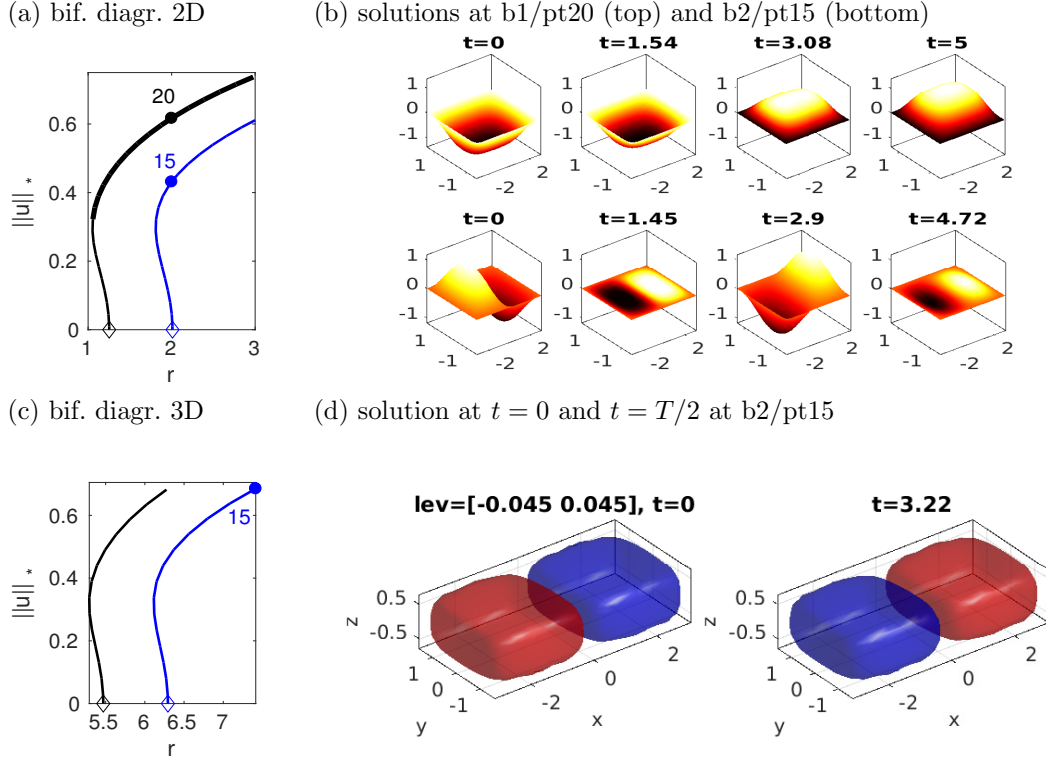


Figure 3: (a) Bifurcation diagrams of the first 2 Hopf branches for (47) in 2D. (b) Solution snapshot from b1/pt20 and b2/pt15, at $t = 0, \frac{4}{19}T, \frac{8}{19}T, \frac{12}{19}T$. (c),(d) Bifurcation diagram and solution snapshot in 3D, $t = 0$ and $t = 9T/19$.

Table 1: Timing (in seconds) and convergence information for (47) in 2D. t_{LU} is the time for computing 20 points on b1 (without Floquet computations) via (36) with LU prefactorization of \mathcal{A} ; t_{GMRES} corresponds to solving via `ilupack` (total time, including preconditioning), and t_{prec} is the time for preconditioning (same preconditioner works for all 20 points). t_H is the time for computing the (leading 20) Floquet multipliers at $r = 2$ via **FA1** (**FA2** is a factor 10 slower). $\delta T|_{r=2}$ is the period minus the period at the coarser mesh, and indicates the convergence. See [Uec18a] and in particular `cmds2d.m` in the demo directory `hopfdemos/cGL` for the precise settings of numerical switches (drop-tolerance for `ilupack` etc).

m	DoF	$t_{LU}(s)$	$t_{GMRES}(s)$	$t_{prec}(s)$	$t_H(s)$	$\delta T_{r=2}$
20	34440	120	50	20	7	*
30	51660	270	65	30	13	-0.038
40	68880	935	120	55	18	-0.013

In 3D, we consider (47) over $\Omega = (-\pi, \pi) \times (-\pi/2, \pi/2) \times (-\pi/4, \pi/4)$. Here we use a *very* coarse tetrahedral mesh of $n_p = 2912$ points, thus 5824 DoF in space. Analytically, the first 2 HBPs are $r_1 = 21/4$ ($k = (1/2, 1, 2)$) and $r_2 = 6$ ($k = (1, 1, 2)$), but with the coarse mesh we numerically

obtain $r_0 = 5.47$ and $r_1 = 6.29$. Again, this can be greatly improved by, e.g., halving the spatial mesh width, but then the Hopf branches become very expensive. Using $m = 20$ (116480 total DoF) and `ilupack`, the computation of the branches (with 15 continuation steps each) in Fig. 3(c) takes about 450 seconds, with 250 seconds for preconditioning¹², and using **FA1** to a posteriori compute the Floquet multipliers about 40 seconds per orbit. Again, on **b1**, $\text{ind}(u_H) = 1$ up to the fold and $\text{ind}(u_H) = 0$ afterwards, while on **b2** $\text{ind}(u_H)$ decreases from 3 to 2 at the fold and to 1 at the end of the branch, and time integration from an IC from **b2** yields convergence to a periodic solution from **b1**.

Additional to the code for the plots in Fig. 2 (and Fig. 3), [Uec18a] explains the basic steps for

- switching to continuation in another parameter,
- ad hoc mesh refinement in t for the arclength parametrization,
- using `pde2path`'s time integration routines to assess the stability of periodic solutions, and in particular obtain the time evolution of perturbations of unstable orbits.

3.2 Spiral waves on a disk

While the Hopf bifurcations presented in §3.1 have been to (standing) oscillatory patterns, another interesting class is the Hopf bifurcation to rotating patterns, in particular to spiral waves. Such spirals are ubiquitous in 2D reaction diffusion problems, see, e.g., [Pis06, CG09]. Over bounded domains, spiral waves are usually found numerically via time integration, see in particular EZSPIRAL [Bar91], with an $\mathcal{O}(1)$ amplitude, i.e., far from bifurcation. On the other hand, the bifurcation of spiral waves from a homogeneous solution is usually analyzed over all of \mathbb{R}^2 , e.g., [KH81, Hag82, Sch98]. Moreover, spiral waves often undergo secondary bifurcations such as drift, meandering and period doubling, see [Bar95, SSW99, SS07] and the references therein. Two exceptions to the rule of finding spirals numerically by time integration are [BE07, Tsa10]. In [BE07] they are found by growing them from a thin annulus towards the core using AUTO, i.e., by continuation in the inner radius of the annulus. Continuation in other parameters is then done as well, but always at $\mathcal{O}(1)$ amplitude. In [Tsa10] rather general $\lambda - \omega$ systems (see (58)) with homogeneous Neumann BC are considered on finite disks, and the existence of spiral waves is shown by a spiral wave ansatz, which lead to 1D ODE boundary value problem, which are treated by a shooting method.

Here we study, on the unit disk, the bifurcation of standing and rotating waves from the zero solution in a slight modification of a real two component reaction diffusion system from [GKS00], see also [GS02, §4.6, §4.7]. The system is somewhat similar to the cGL equation, but with Robin BC. It reads

$$\begin{aligned} \partial_t u &= d_1 \Delta u + (\beta + r)u + v - (u^2 + v^2)(u - \alpha v), \\ \partial_t v &= d_2 \Delta v + rv - u - (u^2 + v^2)(v + \alpha u), \end{aligned} \tag{56}$$

$$\partial_{\mathbf{n}} u + 10u = 0, \quad \partial_{\mathbf{n}} v + 0.01v = 0, \tag{57}$$

where \mathbf{n} is the outer normal, with parameters $\alpha, \beta, r \in \mathbb{R}$ and $d_1, d_2 > 0$. For $\beta = 0$ and $d_1 = d_2$, (56) is a so called $\lambda - \omega$ system [KH81, Hag82, Tsa10], i.e., of the form

$$\partial_t u = d \Delta u + \lambda(z)u - \omega(z)v, \quad \partial_t v = d \Delta v + \omega(z)u + \lambda(z)v, \quad z = u^2 + v^2, \tag{58}$$

which is a prominent class of 2-component reaction diffusion systems (including the cGL equation) yielding spiral waves. For $\beta \neq 0$ and/or $d_1 \neq d_2$ we thus have a perturbed $\lambda - \omega$ system. Additionally, even for $\beta = 0$ and $d_1 = d_2$ the typical $(u, v) \mapsto (-v, u)$ symmetry of $\lambda - \omega$ systems is already broken by the BC (57). We follow [GKS00] and set $\beta = 0.5$ throughout and at first (§3.2.1)

¹²using (36) with LU prefactorization of \mathcal{A} leads to about 1800s runtime, and, importantly, much higher memory requirements of about 13GB instead of 2GB with `ilupack`;

additionally set $\alpha = 0$, $d_1 = 0.01$, $d_2 = 0.015$, and take r as the main bifurcation parameter. Then (§3.2.2) we set $\alpha = 1$, let $(d_1, d_2) = \delta(0.01, 0.015)$, and also vary δ which corresponds to changing the domain size by $1/\sqrt{\delta}$.

The eigenfunctions of the linearization around $(u, v) = (0, 0)$ are build from Fourier Bessel functions

$$\phi_m(\rho, \vartheta, t) = \text{Re}(e^{i(\omega t + m\vartheta)} J_m(q\rho)), \quad m \in \mathbb{Z}, \quad (59)$$

where (ρ, ϑ) are polar-coordinates, and with, due to the BC (57), in general complex $q \in \mathbb{C} \setminus \mathbb{R}$. Then the modes are growing in ρ , which is a key idea of [GKS00] to find modes bifurcating from $(u, v) = (0, 0)$ which resemble spiral waves near their core.

Additional to time translation, the symmetry group of (56),(57) is $O(2)$, acting by rotations and reflections in x . The modes (59) with $m \neq 0$ have the symmetry of rotating waves (RW), and Hopf bifurcations with $m \neq 0$ in (59) are double. The bifurcating branches are branches of clockwise and counterclockwise RW, and branches of standing waves (SW) given by equal amplitude superpositions of clockwise and counterclockwise RW. This follows from the equivariant Hopf theorem, see, e.g., [Hoy06, §4.4 and §5.7], and [GS02, §4.6, 4.7], or [Kno94] and the references therein for earlier and illustrative results in physical applications. For 2π time-periodic solutions (after rescaling t), the equivariance group of (56),(57) is $\Gamma = O(2) \times S^1$, with fixed point subspace $\text{Fix}(\Gamma) = \{u \equiv 0\}$, and an isotropy subgroup is

$$\Sigma_1 = \{\gamma = (\vartheta, \vartheta) : 0 \leq \vartheta < 2\pi\}, \text{ where } U((\vartheta_1, \vartheta_2)(x, t)) = U(R_{\vartheta_1}x, t - \vartheta_2), \quad U = (u, v),$$

with $R_\vartheta = \begin{pmatrix} \cos \vartheta & \sin \vartheta \\ -\sin \vartheta & \cos \vartheta \end{pmatrix}$, i.e., the action of $\gamma \in \Sigma_1$ is rotation in x and time shift by ϑ .

The associated fixed-point subspace $\text{Fix}(\Sigma_1)$ consists of counterclockwise RW, and the conjugate subgroup $\Sigma_2 = \{\gamma = (-\vartheta, \vartheta) : 0 \leq \vartheta < 2\pi\}$ has $\text{Fix}(\Sigma_2)$ consisting of clockwise RW.

Our default branch switching (19) only applies to simple Hopf bifurcations. Nevertheless, if we apply (19) at a double Hopf bifurcation in the present example, then it turns out that the initial guess is sufficiently close to a RW, either from $\text{Fix}(\Sigma_1)$ or from $\text{Fix}(\Sigma_2)$, for the subsequent Newton loop to converge to this RW. On the other hand, to switch to SW, we use a modified ad hoc ansatz

$$u(t) = u_0 + 2\varepsilon\alpha \text{Re}((z_1 e^{-i\omega_H t} + z_2 e^{i\omega_H t})\Psi) \quad (60)$$

with user provided $z_1, z_2 \in \mathbb{C}$, which thus generalizes (19) ($z_1 = 1, z_2 = 0$). Using $z_1 = 1, z_2 = i$ at the HBPs with $m \geq 1$ yields bifurcation to SW. However, the continuation of SW is more expensive than that of RW, because the phase condition (21) fixes the rotational invariance for RW (as time-shifts correspond to rotations), but not for SW. The continuation of SW works, because the FEM discretization destroys the (strict) rotational invariance, but it initially needs small stepsizes due to small eigenvalues, and in the initial continuation steps the orientation of the SW pattern slightly shifts.¹³ Steps towards a more systematic treatment of equivariant Hopf bifurcations are intended for the next version of `pde2path`.

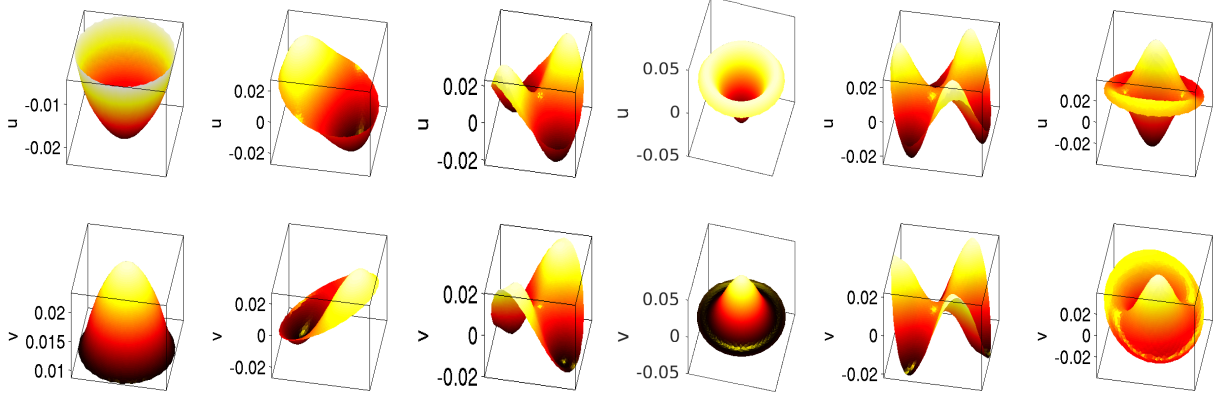
3.2.1 Bifurcations to rotating and standing waves

For $\beta = 0.5$, the trivial homogeneous branch $(u, v) = (0, 0)$ is stable up to $r \approx -0.21$, and Fig. 4(a) shows the spatial modes at the first six Hopf bifurcation points, with mode numbers $m = 0, 1, 2, 0, 3, 2$. (b) shows a basic bifurcation diagram. The RW branches are plotted as full lines, and the standing waves, which for $m = 0$ are also called target patterns, obtained from (60) are plotted as dashed lines. (c) shows selected snapshots of rotating waves from the last points on

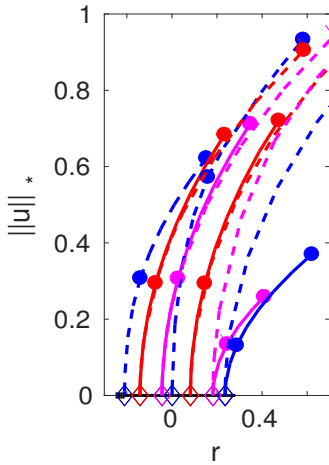
¹³The loss of true rotational invariance can also be seen in the RW, which show small deviations from rigid rotations.

the RW branches in (b), with T near 2π for all branches, while (d) shows similar snapshots from SW branches. We discretized (56), (57) with a mesh of 1272 points, hence $n_u = 2544$ DoF, and a temporal discretization of 15 points, which yields about 1 minute for the computation of each branch, with 10 points on each.

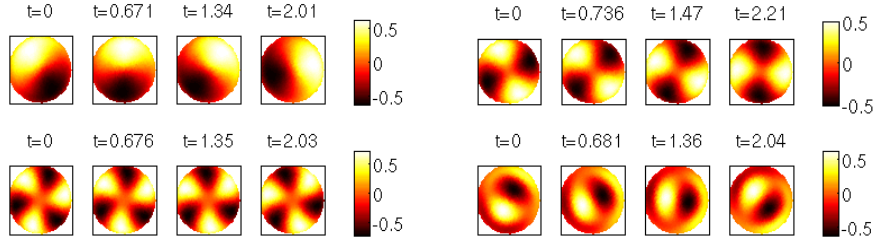
(a) Spatial mode structure at bifurcation, HBP1, ..., HBP6



(b) Bifurcation diagram



(c) snapshots from rotating waves rw2,rw3 (top) and rw5,rw6 (bottom)



(d) snapshots from standing waves sw2 and sw3

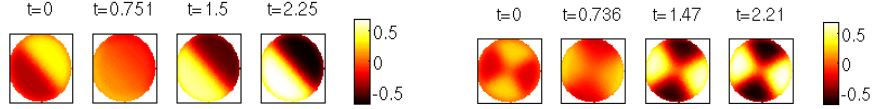


Figure 4: (a) Modes at the first six Hopf bifurcations. (b) Basic bifurcation diagram for rotating waves (full lines rw2, rw3, rw5, rw6, rw7), and standing waves (dashed lines sw1, ..., sw7) for (56), (57), 10 continuation steps for each. On sw1 and the RW branches we mark the points 5 and 10. (c) Snapshots of u from the RW branches at the last points, $t = 0, T_j/9, 2T_j/9, T_j/3$, with T_j the actual period. (d) Snapshots of u from the RW branches sw2 and sw3.

To assess the numerical accuracy, in Table 2 we compare the numerical values for the Hopf points and the temporal wave number ω with the values from [GKS00], who compute HBP5, HBP6, HBP7, (and three more Hopf points at larger r) using semi analytical methods, and some numerics based on the `Matlab pde toolbox` with fine meshes. Given our coarse mesh we find our results reasonably close, and again our values converge to the values from [GKS00] under mesh refinement.

The last two rows of Table 2 give the Floquet indices of points on sw1, sw4, and the RW branches, where err_{γ_1} (cf. (44)) is around 10^{-10} for each computation. All branches except sw1 are unstable, and the instability indices increase from left to right, and also vary along the unstable branches. The stability of sw2, sw3, sw5, sw6, and sw7, is never better than that of the corresponding RW branches, i.e, their index is always at least as large as that of the corresponding RW at the same r

Table 2: Comparison of HBPs with [GKS00] (starred values), and Floquet indices at points on the bifurcating branches (SW (target patterns) for $m = 0$ and RW for $m \neq 0$).

HBP number	HBP1	HBP2	HBP3	HBP4	HBP5	HBP6	HBP7
r	-0.210	-0.141	-0.044	0.001	0.079	0.182	0.236
ω	0.957	0.967	0.965	0.961	0.961	0.953	0.957
m	0	1	2	0	3	1	4
multiplicity	1	2	2	1	2	2	2
r^*	NA	NA	NA	NA	0.080	0.179	0.234
ω^*	NA	NA	NA	NA	0.961	0.953	0.957
$\text{ind}(u_H)$, pt5	0	2	6	12	12	16	20
$\text{ind}(u_H)$, pt10	0	2	4	18	8	18	16

value.

Altogether (56),(57) with $(\alpha, \delta) = (0, 1)$ does not appear to be very interesting from a dynamical and pattern forming point of view, as time-integration yields that for $r > r_0 = -0.21$ solutions to generic initial conditions converge to a periodic orbit from h1. Thus, we next choose $\alpha = 1$ to switch on a rotation also in the nonlinearity, and decrease d_1, d_2 to consider larger domains where the spiral nature of RW becomes more visible.

3.2.2 Spiral waves

We now let $\alpha = 1$ and $(d_1, d_2) = \delta(0.01, 0.015)$. For $(\alpha, \delta) = (1, 1)$ the linearization around $(u, v) = (0, 0)$ is as in in §3.2.1, and thus also yields the same Hopf bifurcation points. However, the nonlinear rotation (due to $\alpha > 0$) yields a spiral wave structure on the branches sp2, sp3, sp5, sp6, and sp7, bifurcating at the points with $m \geq 1$, see Fig. 5(b), where we only give snapshots of $u(\cdot, 0)$, at $r = 1$ and at $r = 3$ for sp2, and at $r = 3$ for the remaining branches.

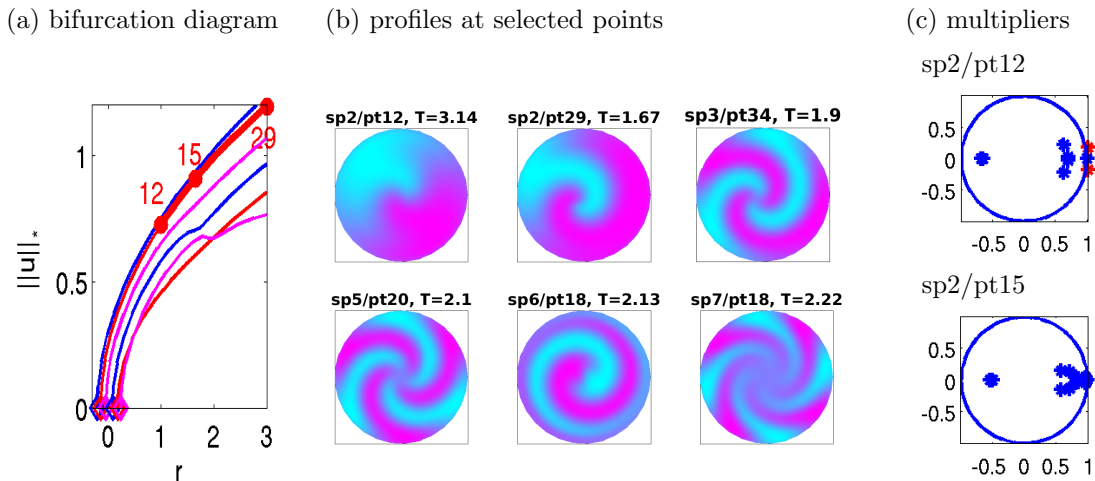


Figure 5: Bifurcation diagram (a) with branches sp1,...,sp7 left to right, and selected profiles (b) and Floquet spectra (c). The (non-rotational) branch sp1 is stable for all r but plotted as a thin line (first blue line in (a)) for graphical reasons. The first two plots in (b) are both from sp2, indicating the more pronounced spiral nature for larger r (on all branches); remaining plots all at $r = 3$. T in (b) indicates the period, which decreases in r and increases with the number m of arms of the spirals.

On sp2, sp3, sp5, and sp7 the solutions rotate in counterclockwise direction with the indicated period T , while on sp6 we have a clockwise rotation. Thus, on sp2, sp3, sp5 and sp7 we have inwardly moving spirals, also called anti-spirals [VE01]. Moreover, again sp1 (with $m = 0$) is stable

for all $r > r_{h1}$, but additionally sp2 becomes stable for $r > r_1 \approx 1$, see Fig. 5(c), while sp4,sp6 and the m -armed spirals with $m > 1$ on sp3, sp5, sp7 are unstable, as should be expected [Hag82]; also note how the core becomes flatter with an increasing number of arms, again cf. [Hag82] and the references therein.

In Fig. 6(a) we first continue (u, v) from sp2 at $r = 3$ in δ to $\delta = 0.1$, i.e., to domain radius $\sqrt{10}$ (branch sp2d). As expected, with the growing domain the spirals become more pronounced. The solutions stay stable down to $\delta = \delta_1 \approx 0.15$, as illustrated in (b). In (c) we continue the solution from sp2d/pt29 (with $\delta = 0.2$) again in r down to $r = r_{h2}^* \approx -0.22$, which is the associated Hopf bifurcation point over a circle of radius $\sqrt{5}$, see also the last plot in (c), which is very close to bifurcation. Now the 1-armed spiral like solution is stable also for rather small amplitude.

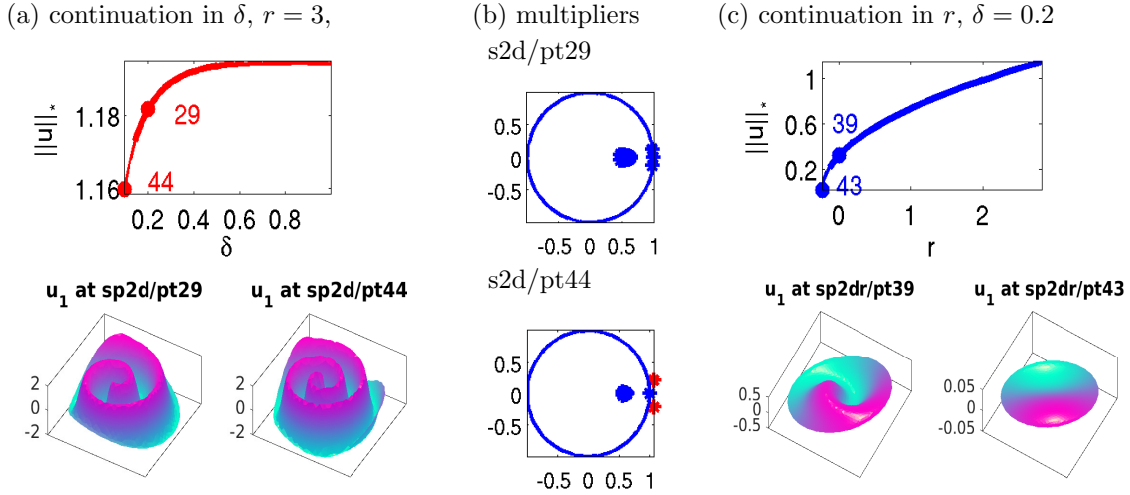


Figure 6: (a) Continuation of the one armed spiral in δ (inverse domain-size). Over a larger domain the spiral nature (of all spirals) is more visible. (b) Multipliers for points in (a). (c) Continuation of pt29 from (a) in r ; over a larger domain the “one-armed spiral” is stable for lower amplitudes.

The model with $(r, \alpha, \delta) = (3, 1, 0.1)$ (and $\beta = 0.5$) is also quite rich dynamically. Besides solutions converging to sp1, the 1-armed spiral sp2 has a significant domain of attraction, but there are also various at least meta-stable solutions, i.e., almost stable solutions with very weakly unstable directions, which consist of long-lived oscillations (with or without rotations). These results fully agree with those from [Tsa10], where the stability of spirals in some cGL-type $\lambda - \omega$ systems on the unit disk is studied by dynamical simulations. Like in our system, the 1-armed spiral waves are unstable at bifurcation and become stable at some finite amplitude (for suitable parameters). See [Uec18a] for comments on how to run such dynamical simulations in `pde2path`.

3.3 An extended Brusselator

As an example with an interesting interplay between stationary patterns and Hopf bifurcations we consider an “extended Brusselator” problem from [YDZE02]. Relatedly, in this example there are many eigenvalues with small real parts, and therefore detecting HBPs without first setting a guess for a shift ω_1 is problematic. The system is given by

$$\partial_t u = D_u \Delta u + f(u, v) - cu + dw, \quad \partial_t v = D_v \Delta v + g(u, v), \quad \partial_t w = D_w \Delta w + cu - dw, \quad (61)$$

where $f(u, v) = a - (1+b)u + u^2v$, $g(u, v) = bu - u^2v$, with kinetic parameters a, b, c, d and diffusion constants D_u, D_v, D_w . We consider (61) on rectangular domains in 1D and 2D, with homogeneous Neumann BC for all three components. The system has the spatially homogeneous steady state

$$U_s = (u, v, w) := (a, b/a, ac/d),$$

and in suitable parameter regimes it shows co-dimension 2 points between Hopf, Turing–Hopf (aka wave), and (stationary) Turing bifurcations from U_s . We follow [YDZE02] and fix the parameters

$$(c, d, D_u, D_v, D_w) = (1, 1, 0.01, 0.1, 1). \quad (62)$$

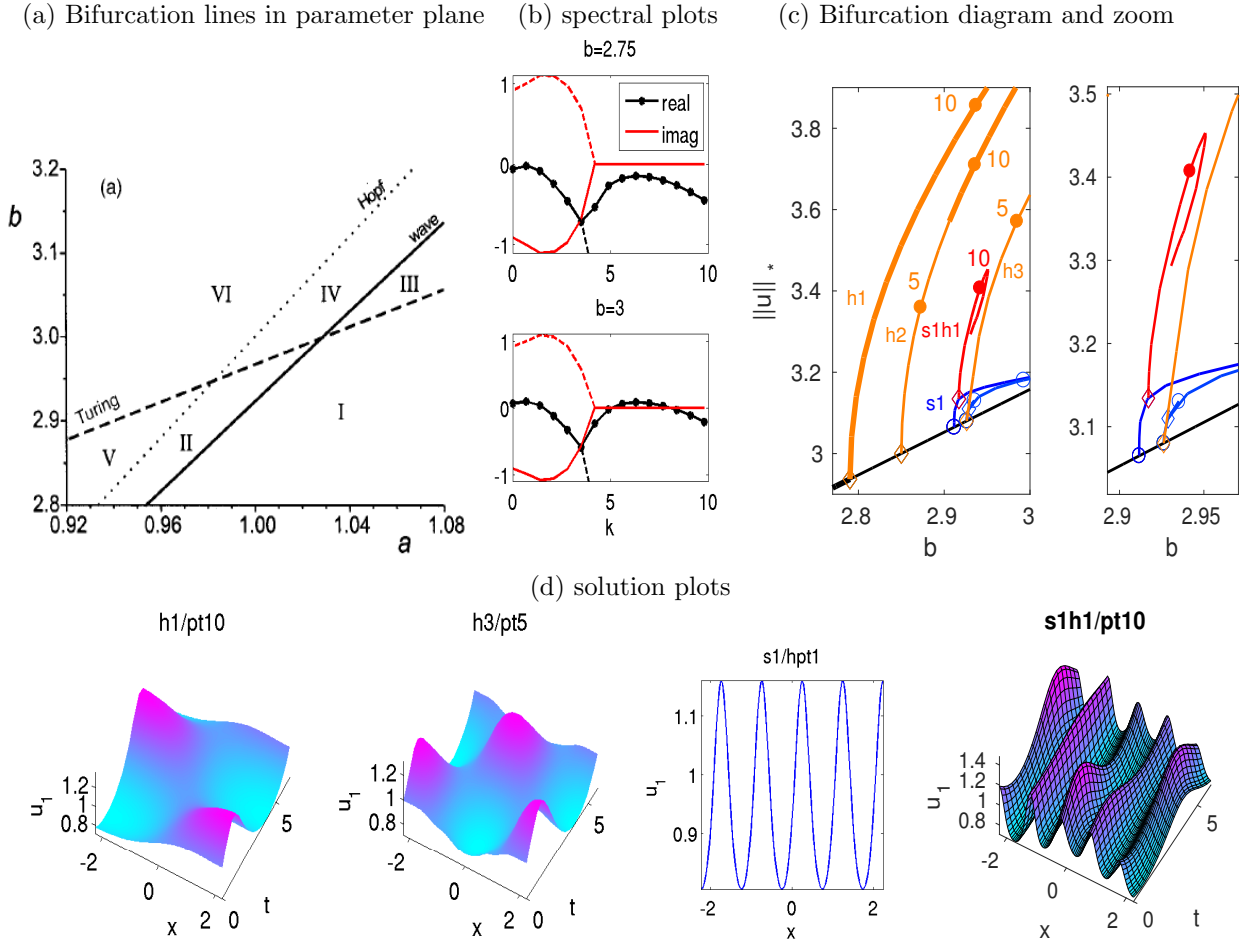


Figure 7: (a) Parameter plane with Hopf, Turing–Hopf (wave) and Turing instability lines for (61), reprinted with permission from [YDZE02], copyright 2002, AIP Publishing LLC. (b) Spectra for increasing b at $a = 0.95$. Contrary to the `pde2path` convention that due to $\partial_t u = -G(u)$ eigenvalues with *negative* real parts yield instabilities, here we directly plot the spectra of $-\partial_u G$, such that instability occurs for eigenvalues with positive real parts. The first instability (Turing–Hopf) occurs at $b \approx 2.794$, with $k_c \approx 0.7$. The admissible wave-numbers k on a domain $(-l_x, l_x)$ with $l_x = 0.5\pi/k_c$ are indicated by the dots. (c) (partial) bifurcation diagram and zoom. (d) example plots. The branches h1,h3 are from Turing Hopf bifurcations, h2 is pure Hopf ($k = 0$), s1 is pure Turing, and in s1h1 we obtain a TH modulation of the s1 Turing pattern.

Figure 7(a) then shows a characterization of the pertinent instabilities of U_s in the a, b plane. U_s is stable in region I, and can loose stability by (a, b) crossing the Turing line, which yields the bifurcation of stationary Turing patterns, or the wave (or Turing–Hopf) line, which yields oscillatory Turing patterns. Moreover, there is the “Hopf line” which corresponds to Hopf–bifurcation with spatial wave number $k = 0$.¹⁴

In the following we fix $a = 0.95$ and take b as the primary bifurcation parameter. Figure 7(b) illustrates the different instabilities from (a). As we increase b from 2.75, we first cross the Turing–

¹⁴See also [Uec18a] for new functions for the computation of these lines by branch point continuation and Hopf point continuation in `pde2path`.

Hopf line, with first instability at critical spatial wave number $k_{\text{TH}} \approx 0.7$, then the Hopf line, and finally the Turing line with critical wave number $k_{\text{T}} \approx 6.4$. To investigate the bifurcating solutions (and some secondary bifurcations) with `pde2path`, we need to choose a domain $\Omega = (-l_x/2, l_x/2)$ (1D), where due to the Neumann BC l_x should be chosen as a (half integer) multiple of π/k_{TH} . For simplicity we take the minimal choice $l_x = 0.5\pi/k_{\text{TH}}$, which restricts the allowed wave numbers to multiples of k_{TH} , as indicated by the black dots in Figure 7(b). Looking at the sequence of spectral plots for increasing b , we may then expect first the Turing–Hopf branch h1 with $k = k_{\text{TH}}$, then a Hopf branch h2 with $k = 0$, then two Turing branches s1 , s2 with $k = 6.3$ and $k = 7$, then a Turing–Hopf branch h3 with $k = 2k_{\text{TH}}$, and so on, and this is what we obtain from the numerics, as illustrated in (c) and (d), using a coarse mesh with 101 grid points, hence $3 \times 101 = 303$ DoF in space.

Besides stationary secondary bifurcations we also get a rather large number of Hopf points on the Turing branches, and just as an example we plot the (Turing)Hopf branch s1h1 bifurcating from the first Hopf point on s1 . The example plots in (d) illustrate that solutions on s1h1 look like a superposition of solutions on s1 and h1 . Such solutions were already obtained in [YDZE02] from time integration, which is only possible because some solutions of this kind are stable, see also [YE03] for similar phenomena. By following the model’s various bifurcations, this can be studied in a more systematic way.

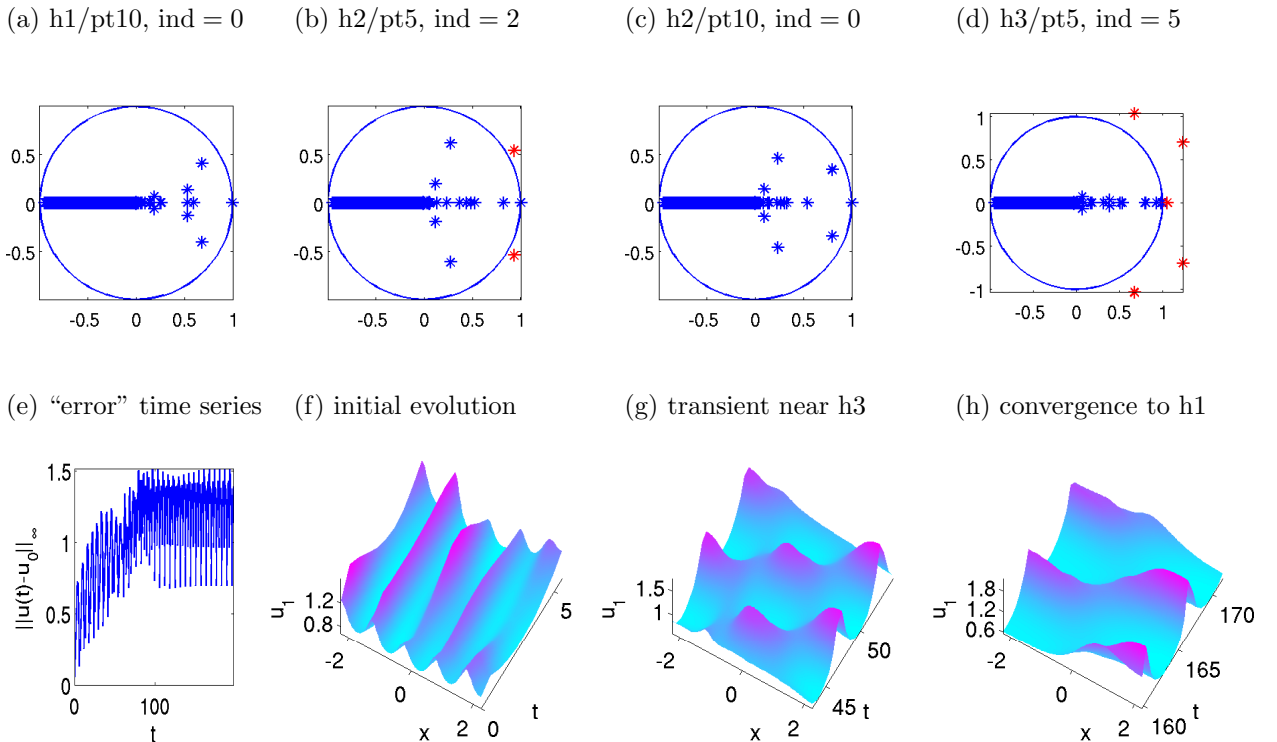


Figure 8: (a)-(d) A small sample of Floquet spectra of periodic orbits from Fig. 7 (200 largest multipliers computed via `floq`), illustrating that a Neimark–Sacker bifurcation should be expected near $\text{h2}/\text{pt5}$, and similar eigenvalue transitions occur on all other Hopf branches except h1 . (e)-(h) Evolution of a perturbation of $\text{s1h1}/\text{pt10}$. After a rather long transient near h3 the solution converges to an orbit on h1 .

It turns out that h1 is stable up to rather large amplitude¹⁵, and that (the spatially homogeneous branch) h2 is initially unstable with $\text{ind}(u_H) = 2$, but close to pt5 on h2 we find a Neimark–Sacker bifurcation, after which solutions on h2 are stable. Similarly, solutions on h3 start with $\text{ind}(u_H) = 5$,

¹⁵see [Uec18a] for the (pitchfork) bifurcations from h1 occurring near $b = 3.01$ and $b = 3.15$, and the continuation of the periodic orbits bifurcating there

but after a Neimark–Sacker bifurcation, and a real multiplier going through 1 at $b \approx 3.35$ we find $\text{ind}(u_H) = 2$, before $\text{ind}(u_H)$ increases again for larger b . Also note that there are always many multipliers close to -1 , but we did not find indications for period–doubling bifurcations. Finally, in Fig. 8(e)–(h) we illustrate the evolution of perturbations of `s1h1/pt10`. After a transient near `h3/pt5` (g) the solution converges to a solution from the primary Hopf branch `h1` (h), which however itself also shows some short wave structure at this relatively large distance from bifurcation.

In 1D we may still use **HD1** to detect (and localize) the Hopf bifurcations. In 2D this is unfeasible, because even over small domains we obtain many wave vectors $k = (k_1, k_2)$ with modulus $|k| \in (5, 8)$, which give leading eigenvalues $\mu_1(k)$ with small $\text{Re}\mu(k)$ and $\text{Im}\mu(k) = 0$. This is illustrated in Fig. 9, which shows that for $\Omega = (-0.5\pi/k_{\text{TH}}, 0.5\pi/k_{\text{TH}})^2$ even for $n_{\text{eig}} = 200$ (which is quite slow already) we do not even see any Hopf eigenvalues, which become “visible” at, e.g., $n_{\text{eig}} = 300$. Thus, here we use **HD2** which runs fast and reliably, even with just computing 3 eigenvalues both near 0 and ω_1 , obtained from (14).

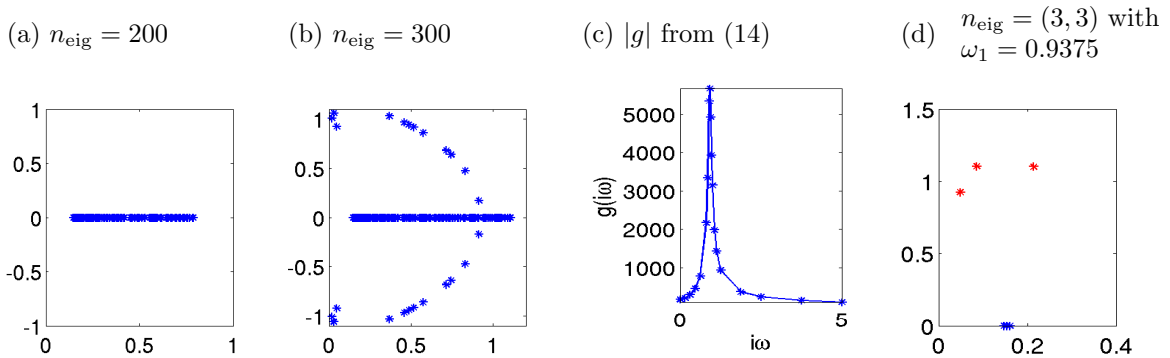


Figure 9: (a,b) n_{eig} smallest eigenvalues of the linearization of (61) around U_s at $b = 2.75$, remaining parameters from (62); **HD1** with $n_{\text{eig}} = 200$ will not detect any Hopf points. (c) (14) yields a guess $\omega_1 = 0.9375$ for the ω value at Hopf bifurcation, and then **HD2** with $n_{\text{eig}} = (3, 3)$ is reliable and fast: (d) shows the three eigenvalues closest to 0 in blue, and the three eigenvalues closest to $i\omega_1$ in red.

In Fig. 10 we give examples of just four of the many branches which can be obtained for (61) in 2D, even over quite small domains. We use $\Omega = (-l_x, l_x) \times (-l_y, l_y)$, $l_x = \pi/2$, $l_y = \pi/8$, with a mesh of 961 gridpoints, hence 2883 spatial degrees of freedom, and for the Hopf orbits we use 15 gridpoints in t . The domain means that admissible wave vectors are $(k_1, k_2) = (n, 4m)$, $n, m \in \mathbb{N}_0$. Consequently, no spatial structure in y direction occurs in the primary Hopf branches (cf. Fig. 7b), i.e., the first three are just analogous to those in Fig. 7 and occur at $b = 2.818$ (with $k = (1, 0)$), $b = 2.859$ (with $k = (0, 0)$, i.e., spatially homogeneous, and hence b independent of the domain) and $b = 3.202$ (with $k = (2, 0)$); see (b1) for an example plot on the first Hopf branch. The first stationary bifurcation (at $b = 2.912$) is now to a spotted branch `2ds1`, and stripe branches analogous to `s1` from Fig. 7 bifurcate at larger b . Interestingly, after some stationary and Hopf bifurcations the `2ds1` branch becomes stable at $b = b_b \approx 2.785$, which illustrates that it is often worthwhile to follow unstable branches, as they may become stable, or stable branches may bifurcate off.¹⁶ Figure 10(b2) shows an example plot from the first secondary Hopf branch. This is analogous to `s1h1` from Fig. 7, i.e., the solutions look like superpositions of the stationary pattern and solutions on the primary Hopf branch `h1`.

Concerning the multipliers we find that $\text{ind}(u_H) = 0$ on `2dh1`, and, e.g., $\text{ind}(u_H) = 5$ at `2ds1h1/pt5`, where as in 1D (Fig. 9) there are multipliers suggesting Neimark–Sacker bifurcations. Figure 10 (c) illustrates the instability of the spotted Hopf solutions; the spots stay visible for

¹⁶For continuing this branch we also use a few additional features of `pde2path` such as adaptive spatial mesh-refinement and `pmcont`, see [Uec18a]

about 4 periods, and subsequently the solution converges to a periodic orbit from the primary Hopf branch, as in Fig. 8.

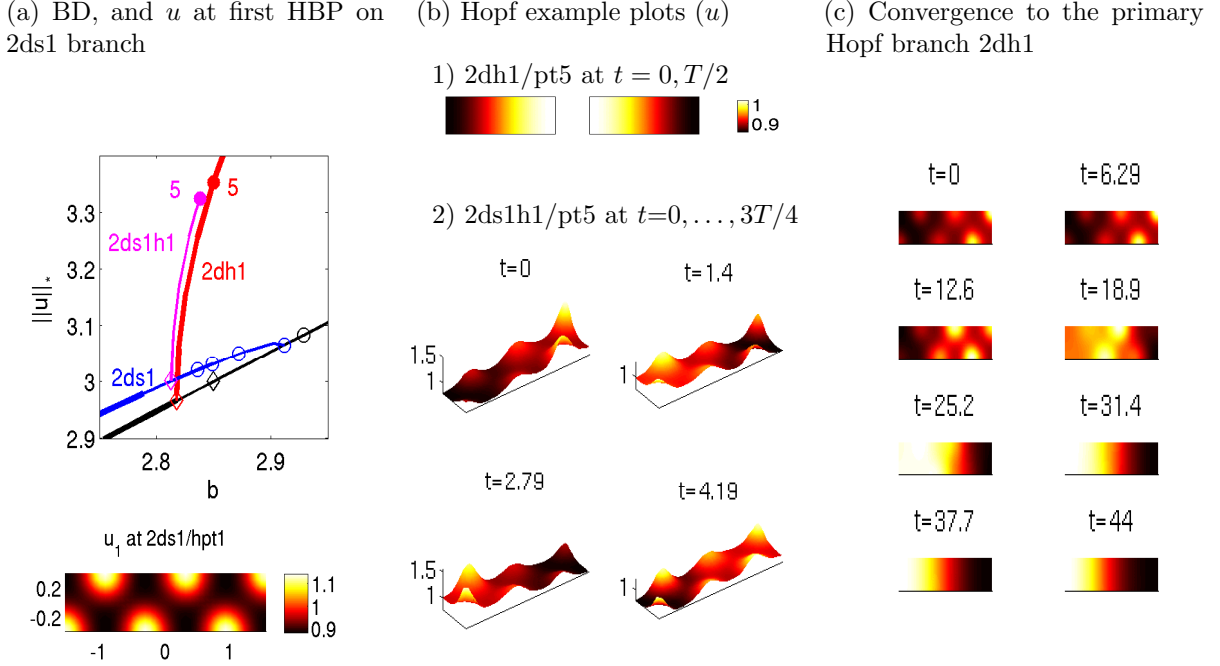


Figure 10: (a) Example bifurcations for (61) over a small 2D domain $\Omega = (-\pi/2, \pi/2) \times (-\pi/8, \pi/8)$, and example plots of u at 2nd Hopf point on the blue branch. (b) Example plots: solutions on primary Hopf branch (1), and on the secondary Hopf branch (2) (the amplitude at $t = 1.4$ and $t = 4.19$ is about 0.2). (c) Time integration with $u(\cdot, 0)$ from 2ds1h1/pt5, snapshots at $0, T, 2T, \dots, 8T$.

3.4 A canonical system from optimal control

In [Uec16, GU17], `pde2path` has been used to study so called canonical steady states and canonical paths for infinite time horizon distributed optimal control (OC) problems. As an example for such problems with Hopf bifurcations we consider

$$V(v_0(\cdot)) \stackrel{!}{=} \max_{k(\cdot, \cdot)} J(v_0(\cdot), k(\cdot, \cdot)), \quad J(v_0(\cdot), k(\cdot, \cdot)) := \int_0^\infty e^{-\rho t} J_{ca}(v(t), k(t)) dt, \quad (63a)$$

where $J_{ca}(v(\cdot, t), k(\cdot, t)) = \frac{1}{|\Omega|} \int_\Omega J_c(v(x, t), k(x, t)) dx$ is the spatially averaged current value function, with

$$J_c(v, k) = pv_1 - \beta v_2 - C(k) \text{ the local current value, } C(k) = k + \frac{1}{2\gamma} k^2, \quad (63b)$$

where $\rho > 0$ is the discount rate (long-term investment rate), and where the state evolution is

$$\partial_t v_1 = -k + d_1 \Delta v_1, \quad \partial_t v_2 = v_1 - \alpha(v_2) + d_2 \Delta v_2, \quad \alpha(v_2) = v_2(1 - v_2) \quad (63c)$$

with Neumann BC $\partial_n v = 0$ on $\partial\Omega$. Here, $v_1 = v_1(t, x)$ are the emissions of some firms, $v_2 = v_2(t, x)$ is the pollution stock, and the control $k = k(t, x)$ models the firms' abatement policies.¹⁷ The terms

¹⁷We use the letter k for the control instead of the more custom u , because $u = (v_1, v_2, \lambda_1, \lambda_2)$ shall denote the vector of states (v_1, v_2) and co-states (λ_1, λ_2) .

pv_1 and βv_2 in J_c are the firms' value of emissions and costs of pollution, $C(k)$ are the costs for abatement, and $\alpha(v_2)$ is the recovery function of the environment. The discounted time integral in (63a) is typical for economic problems, where "profits now" weight more than mid or far future profits. Finally, the max in (63a) runs over all *admissible* controls k ; this essentially means that $k \in L^\infty((0, \infty) \times \Omega, \mathbb{R})$, and we do not consider active control or state constraints.

The associated ODE OC problem (no x -dependence of v, k) was set up and analyzed in [TW96, Wir00]; in suitable parameter regimes it shows Hopf bifurcations of periodic orbits for the associated so called canonical (ODE) system. See also, e.g., [DF91, Wir96, GCF⁺08] for general results about the occurrence of Hopf bifurcations and optimal periodic solutions in ODE OC problems.

Setting $g_1(v, k) = (-k, v_1 - \alpha(v_2))^T$, $D = \text{diag}(d_1, d_2)$, and introducing the co-states (Lagrange multipliers)

$$\lambda : \Omega \times (0, \infty) \rightarrow \mathbb{R}^2,$$

we define the (local current value) Hamiltonian $\mathcal{H} = \mathcal{H}(v, \lambda, k) = J_c(v, k) + \langle \lambda, D\Delta v + g_1(v, k) \rangle$, where $\langle \lambda, v \rangle = \lambda_1 v_1 + \lambda_2 v_2$ denotes the standard scalar product in \mathbb{R}^2 . By Pontryagin's Maximum Principle for

$$\tilde{\mathcal{H}} = \int_0^\infty e^{-\rho t} \bar{\mathcal{H}}(t) dt \quad \text{with} \quad \bar{\mathcal{H}}(t) = \int_\Omega \mathcal{H}(v(x, t), \lambda(x, t), k(x, t)) dx,$$

an optimal solution (v, λ) has to solve the canonical system (first order necessary optimality conditions)

$$\partial_t v = \partial_\lambda \mathcal{H} = D\Delta v + g_1(v, k), \quad v|_{t=0} = v_0, \quad (64a)$$

$$\partial_t \lambda = \rho \lambda - \partial_v \mathcal{H} = \rho \lambda + g_2(v, k) - D\Delta \lambda, \quad (64b)$$

where $\partial_n \lambda = 0$ on $\partial\Omega$, and $g_2 = (\partial_v g_1)\lambda = (-p - \lambda_2, \alpha'(v_2)\lambda_2 + \beta)$. The control k fulfills $k = \arg\max_{\tilde{k}} \mathcal{H}(v, \lambda, \tilde{k})$. Under suitable concavity assumptions on J_c , and in the absence of control constraints, k is obtained from solving $\partial_k \mathcal{H}(v, \lambda, k) = 0$, thus here

$$k = k(\lambda_1) = -(1 + \lambda_1)/\gamma. \quad (65)$$

Remark 3.1. The use of the Hamiltonian $\tilde{\mathcal{H}}$ is the standard way of dealing with intertemporal OC problems in economics. Equivalently, the canonical system (64) is formally obtained as the first variation of the Lagrangian

$$\mathcal{L} = \frac{1}{|\Omega|} \int_0^\infty e^{-\rho t} \left(\int_\Omega J_c(v, k) - \langle \lambda, \partial_t v + G_1(v, k) \rangle dx \right) dt, \quad (66)$$

where $G_1(v, k) = -D\Delta v - g_1$, and where $\lambda = (\lambda_1, \lambda_2)$ can directly be identified as Lagrange multipliers to the constraint (63c), i.e., $\partial_t v + G_1(v, k) = 0$. Using integration by parts in x with the Neumann BC $\partial_n v = 0$ and $\partial_n \lambda = 0$ we have $\int_\Omega \langle \lambda, D\Delta v \rangle dx = \int_\Omega \langle D\Delta \lambda, v \rangle dx$, and using integration by parts in t with the intertemporal transversality condition

$$\lim_{t \rightarrow \infty} e^{-\rho t} \int_\Omega \langle v, \lambda \rangle dx = 0 \quad (67)$$

yields $-\int_0^\infty e^{-\rho t} \int_\Omega \langle \lambda, \partial_t v \rangle dx dt = \int_\Omega \langle \lambda(x, 0), v(x, 0) \rangle dx + \int_0^\infty e^{-\rho t} \langle \partial_t \lambda - \rho \lambda, v \rangle dx dt$. Thus, \mathcal{L} can also be written as

$$\begin{aligned} \mathcal{L} = & \frac{1}{|\Omega|} \left[\int_\Omega \langle \lambda(x, 0), v(x, 0) \rangle dx \right. \\ & \left. + \int_0^\infty e^{-\rho t} \left(\int_\Omega J_c(v, k) + \langle \partial_t \lambda + \rho \lambda + D\Delta \lambda, v \rangle + \langle \lambda, g_1(v, k) \rangle dx \right) dt \right], \end{aligned} \quad (68)$$

and (64) are the first variations of \mathcal{L} with respect to λ (using (66)) and v (using (68)) with $v(0, x) = v_0(x)$. However, both computations (with $\tilde{\mathcal{H}}$ and \mathcal{L}) are somewhat formal, and the rigorous necessity of canonical systems such as (64) for infinite time horizons, and in particular the transversality condition (67), are matters of active research; see, e.g., [AV12, Tau15, GU17] and the references therein. \square

Clearly, (64) is ill-posed as an initial value problem due to the backward diffusion in the co-states λ . Thus it seems unlikely that periodic orbits for (64) can be obtained via shooting methods. For convenience we set $u(t, \cdot) := (v(t, \cdot), \lambda(t, \cdot)) : \Omega \rightarrow \mathbb{R}^4$, and write (64) as

$$\partial_t u = -G(u) := \mathcal{D}\Delta u + f(u), \quad (69)$$

where $\mathcal{D} = \text{diag}(d_1, d_2, -d_1, -d_2)$, $f(u) = (-k, v_1 - \alpha(v_2), \rho\lambda_1 - p - \lambda_2, (\rho + \alpha'(v_2))\lambda_2 + \beta)^T$.

A solution u of the canonical system (69) is called a *canonical path*, and a steady state of (69) (which automatically fulfills (67)) is called a *canonical steady state (CSS)*. A first step for OC problems of type (63) is to find canonical steady states and canonical paths connecting to some CSS u^* . To find such connecting orbits to u^* we may choose a cut-off time T_1 and require that $u(\cdot, T_1)$ is in the stable manifold $W_s(u^*)$ of u^* , which we approximate by the associated stable eigenspace $E_s(u^*)$. If we consider (64) after spatial discretization, then, since we have $n_u/2$ initial conditions, this requires that $\dim E_s(u^*) = n_u/2$. Defining the defect $d(u^*)$ of a CSS as

$$d(u^*) = \frac{n_u}{2} - \dim E_s(u^*), \quad (70)$$

it turns out (see [GU17, Appendix A]) that always $d(u^*) \geq 0$, and we call a u^* with $d(u^*) = 0$ a saddle-point CSS. See [GCF⁺08, GU17] for more formal definitions, and further comments on the notions of optimal systems, the significance of the transversality condition (67), and the (mesh-independent) defect $d(u^*)$. For a saddle point CSS u^* we can then compute canonical paths to u^* , and this has for instance been carried out for a vegetation problem in [Uec16], with some surprising results, including the bifurcation of patterned *optimal* steady states and associated patterned optimal paths.

A natural next step is to search for time-periodic solutions u_H of canonical systems, which obviously also fulfill (67). The natural generalization of (70) is

$$d(u_H) = \text{ind}(u_H) - \frac{n_u}{2}. \quad (71)$$

In the (low-dimensional) ODE case, there then exist methods to compute connecting orbits to (saddle point) periodic orbits u_H with $d(u_H) = 0$, see [BPS01, GCF⁺08], which require comprehensive information on the Floquet multipliers and the associated eigenspace of u_H . Our (longer term) aim is to extend these methods to periodic orbits of PDE OC systems.

However, a detailed numerical analysis of (63) and similar PDE optimal control problems with Hopf bifurcations, and economic interpretation of the results, will appear elsewhere. Here we only illustrate that

- Hopf orbits can appear as candidates for optimal solutions in OC problems of the form (63),
- the computation of multipliers via the periodic Schur decomposition (**FA2**) can yield accurate results, even when the computation directly based on the product (43) (**FA1**) completely fails.

For all parameter values, (69) has the spatially homogeneous CSS

$$u^* = (z_*(1 - z_*), z_*, -1, -(p + \rho)), \quad \text{where} \quad z_* = \frac{1}{2} \left(1 + \rho - \frac{\beta}{p + \rho} \right).$$

We use similar parameter ranges as in [Wir00], namely

$$(p, \beta, \gamma) = (1, 0.2, 300), \quad \text{and} \quad \rho \in [0.5, 0.65] \quad \text{as a continuation parameter,} \quad (72)$$

consider (69) over $\Omega = (-\pi/2, \pi/2)$, and set the diffusion constants to $d_1 = 0.001, d_2 = 0.2$.¹⁸

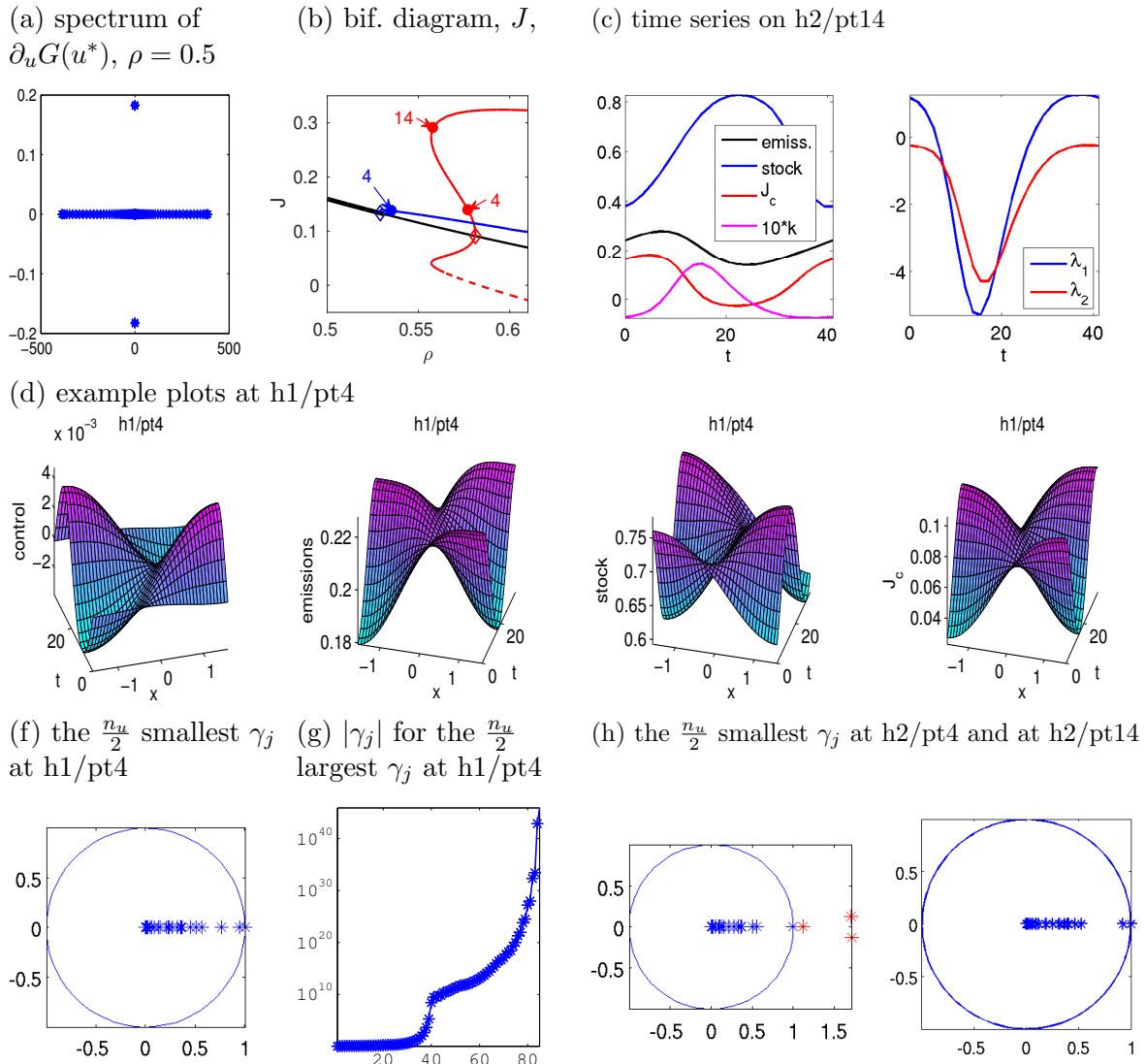


Figure 11: (a) full spectrum of the linearization of (69) around u^* at $\rho = 0.5$ on a coarse mesh with $n_p = 17$. (b) Bifurcation diagram, value J over ρ . Black: u^* ; blue: h1, red: h2, $J(u^H; 0)$ (full line) and $J(u^H; T/2)$ (dashed line). (c) Time series of a spatially homogeneous solution, including current value J_c , control k , and co-states $\lambda_{1,2}$. (d,f,g) Example plots and multipliers of u_H at h1/pt4, which shows that $\text{ind}(u_H) = 0$. (h) multipliers at h2/pt4, which shows that $\text{ind}(u_H) = 3$ at this point, while solutions on h2 become saddles after the fold.

In Figure 11 we give some basic results for (69) with a spatial mesh of $n_p = 41$ points (and thus $n_u = 164$). (a) shows the full spectrum of the linearization of (69) around u^* at $\rho = 0.5$, illustrating the ill-posedness of (69) as an initial value problem. (b) shows a basic bifurcation diagram. At $\rho = \rho_1 \approx 0.53$ a Hopf branch h1 with spatial wave number $l = 1$ bifurcates, and at $\rho = \rho_2 \approx 0.58$

¹⁸The motivation for this choice is to have the first (for increasing ρ) Hopf bifurcation to a spatially patterned branch, and the second to a spatially uniform Hopf branch, because the former is more interesting. We use that the HBPs for the model (69) can be analyzed by a simple modification of [Wir00, Appendix A]. We find that for branches with spatial wave number $l \in \mathbb{N}$ the necessary condition for Hopf bifurcation, $K > 0$ from [Wir00, (A.5)], becomes $K = -(\alpha' + d_2 l^2)(\rho + \alpha' + d_2 l^2) - d_1 l^2(\rho + d_1 l^2) > 0$. Since $\alpha' = \alpha'(z_*) < 0$, a convenient way to first fulfill $K > 0$ for $l = 1$ is to choose $0 < d_1 \ll d_2 < 1$, such that for $l = 0, 1$ the factor $\rho + \alpha' + d_2 l^2$ is the crucial one.

a spatially homogeneous ($l = 0$) Hopf branch **h2** bifurcates and shows a fold at $\rho = \rho_f \approx 0.55$. (c) shows the pertinent time series on **h2/pt14**. As should be expected, J_c is large when the pollution stock is low and emissions are high, and the pollution stock follows the emissions with some delay.

Since ultimately we are interested in the values J of solutions of (69), in (b) we plot J over ρ . For the CSS u^* this is simply $J(u^*) = \frac{1}{\rho} J_{c,a}(u^*)$, but for the periodic orbits we have to take into account the phase, which is free for (69). If u_H is a time periodic solution of (69), then, for $\phi \in [0, T)$, we consider

$$J(u_H; \phi) := \int_0^\infty e^{-\rho t} J_{c,a}(u_H(t + \phi)) dt = \frac{1}{1 - e^{-\rho T}} \int_0^T e^{-\rho t} J_{c,a}(u_H(t + \phi)) dt,$$

which in general may depend on the phase, and for **h2** in (c) we plot $J(u_H; \phi)$ for $\phi = 0$ (full red line) and $\phi = T/2$ (dashed red line). For the spatially periodic branch **h1**, $J_{c,a}(t)$ averages out in x and hence $J(u_H; \phi)$ only weakly depends on ϕ . Thus, we first conclude that for $\rho \in (\rho_1, \rho_f)$ the spatially patterned periodic orbits from **h1** give the highest J , while for $\rho \geq \rho_f$ this is obtained from **h2** with the correct phase. The example plots (c) at **h1/pt4** illustrate how the spatio-temporal dependence of k should be chosen, and the resulting behaviors of v and J_c .

It remains to compute the defects $d(u^*)$ of the CSS and $d(u_H)$ of periodic orbits on the bifurcating branches. For $d(u^*)$ we find that it starts with 0 at $\rho = 0.5$, and, as expected, increases by 2 at each Hopf point. On the Hopf branches we always have $n_+ \geq n_u/2$ unstable multipliers (computed with **FA2**, which yields $\text{err}_{\gamma_1} < 10^{-8}$ for all computations, and hence we trust it), and the leading multipliers are very large, i.e., on the order of 10^{40} , even for the coarse space discretization. Thus, we may expect **FA1** to fail, and indeed it does so completely. For instance, calling `f1oq` to compute all multipliers typically returns 10 and larger for the modulus of the *smallest* multiplier (which from **FA2** is on the order of 10^{-25}).

On **h1** we find $d(u_H) = 0$ up to **pt4**, see (e) for the $n_u/2$ smallest multipliers, and (f) for $|\gamma_j|$ for the large ones, which are mostly real, and $d(u_H) \geq 1$ for larger ρ . On **h2** we start with $d(u_H) = 3$, see (h), but $d(u_H) = 0$ after the fold until $\rho = \rho_1 \approx 0.6$, after which $d(u_H)$ increases again by multipliers going through 1. Since on **h1** we have that $J(u_H)$ is larger than $J(u^*)$, and since u_H is a saddle point up to **pt4**, we expect that these u_H are at least locally optimal, and similarly we expect u_H from **h2** after the fold until ρ_1 to be locally, and probably globally, optimal. However, as already said, for definite answers and, e.g., to characterize the domains of attractions, we need to compute canonical paths connecting to these periodic orbits, and this will be studied elsewhere.

4 Summary and outlook

With the `hopf` library of `pde2path` we provide some basic functionality for Hopf bifurcations and periodic orbit continuation for the class (3) of PDEs over 1D, 2D and 3D domains. The user interfaces reuse the standard `pde2path` setup, and no new user functions are necessary. For the detection of Hopf points we check for eigenvalues crossing the imaginary axis near guesses $i\omega_j$, where the ω_j can either be set by the user (if such a priori information is available), or can be estimated using the function `g` from (14). An initial guess for a bifurcating periodic orbit is then obtained from the normal form (15), and the continuation of the periodic orbits is based on modifications of routines from TOM [MT04].

Floquet multipliers of periodic orbits can be computed from the monodromy matrix \mathcal{M} (43) (**FA1**), or via a periodic Schur decomposition of the block matrices of \mathcal{M} (**FA2**). The former is suitable for dissipative systems, and computes a user chosen number of largest multipliers of \mathcal{M} . This definitely fails for problems of the type considered in §3.4, and in general we recommend to monitor $\text{err}_{\gamma_1} = |\gamma_1 - 1|$ to detect further possible inaccuracies. The periodic Schur decomposition is expensive, but has distinct advantages: It can be used to efficiently compute eigenspaces at all

time-slices and hence bifurcation information in case of critical multipliers, and, presently most importantly for us, it accurately (measured by err_{γ_1}) computes the multipliers also for ill posed problems.

We tested our algorithms on four example problems, where we believe that the second, third and fourth are close to interesting research problems. For instance, in §3.4 we give an outlook on the widely unexplored field of Hopf bifurcations and time periodic orbits in infinite time horizon distributed optimal control PDE problems. For this, as a next step we plan to implement routines to compute canonical paths connecting to periodic orbits. Another important point on our agenda are the branch switching at multiple Hopf points, see Remark 2.1. For the example (56),(57), we so far treat the bifurcations from double Hopf points under $O(2)$ symmetry only in an ad hoc way.

Note added in proof (August 31, 2018). A number of further algorithms is now implemented in `pde2path`, namely: Hopf- and branch point localization and continuation via extended systems, and simple methods for bifurcation from periodic orbits. Besides the application to (61), see footnotes 14 and 15, [Uec18a] also contains an example of a period doubling bifurcation of breathers. Further examples how to treat bifurcations with continuous symmetries in `pde2path` are also given in [RU17] and [Uec18a].

References

- [AK02] I. S. Aranson and L. Kramer. The world of the complex Ginzburg-Landau equation. *Rev. Modern Phys.*, 74(1):99–143, 2002.
- [AV12] S. Aseev and V. Veliov. Maximum principle for infinite-horizon optimal control problems with dominating discount. *Dyn. Contin. Discrete Impuls. Syst. Ser. B*, 19(1-2):43–63, 2012.
- [Bar91] D. Barkley. A model for fast computer simulation of waves in excitable media. *Physica D*, 49:61–70, 1991.
- [Bar95] D. Barkley. Spiral meandering. In *Chemical Waves and Patterns*, edited by R. Kapral and K. Showalter. Kluwer, 1995.
- [BE07] G. Bordyugov and H. Engel. Continuation of spiral waves. *Physica D*, 228(1):49–58, 2007.
- [BFG⁺14] D. Bindel, M. Friedman, W. Govaerts, J. Hughes, and Yu.A. Kuznetsov. Numerical computation of bifurcations in large equilibrium systems in matlab. *J. Comput. Appl. Math.*, 261:232–248, 2014.
- [BGVD92] A. Bojanczyk, G.H. Golub, and P. Van Dooren. The periodic Schur decomposition; algorithm and applications. In *Proc. SPIE Conference, Volume 1770*, pages 31–42. 1992.
- [Bol11] M. Bollhöfer. ILUPACK V2.4, www.icm.tu-bs.de/~bolle/ilupack/, 2011.
- [BPS01] W.J. Beyn, Th. Pampel, and W. Semmler. Dynamic optimization and Skiba sets in economic examples. *Optimal Control Applications and Methods*, 22(5–6):251–280, 2001.
- [BT07] W.J. Beyn and V. Thümmler. Phase conditions, symmetries, and PDE continuation. In *Numerical continuation methods for dynamical systems*, pages 301–330. Springer, Dordrecht, 2007.
- [CG09] M. Cross and H. Greenside. *Pattern Formation and Dynamics in Nonequilibrium Systems*. Cambridge University Press, 2009.
- [DCF⁺97] E. Doedel, A. R. Champneys, Th. F. Fairgrieve, Y. A. Kuznetsov, Bj. Sandstede, and X. Wang. AUTO: Continuation and bifurcation software for ordinary differential equations (with Hom-Cont). <http://indy.cs.concordia.ca/auto/>, 1997.
- [DF91] E. Dockner and G. Feichtinger. On the optimality of limit cycles in dynamic economic systems. *Journal of Economics*, 53:31–50, 1991.

- [DGK03] A. Dhooge, W. Govaerts, and Yu.A. Kuznetsov. MATCONT: a matlab package for numerical bifurcation analysis of ODEs. *ACM Trans. Math. Software*, 29:141–164, 2003.
- [DGK⁺08] A. Dhooge, W. Govaerts, Yu.A. Kuznetsov, W. Mestrom, and A.M. Riet. CL_MATCONT. www.sourceforge.net/projects/matcont/, 2008.
- [Doe07] E. J. Doedel. Lecture notes on numerical analysis of nonlinear equations. In *Numerical continuation methods for dynamical systems*, pages 1–49. Springer, Dordrecht, 2007.
- [DRUW14] T. Dohnal, J.D.M. Rademacher, H. Uecker, and D. Wetzel. pde2path 2.0. In H. Ecker, A. Steindl, and S. Jakubek, editors, *ENOC 2014 - Proceedings of 8th European Nonlinear Dynamics Conference*, ISBN: 978-3-200-03433-4, 2014.
- [DS13] H. Dankowicz and Fr. Schilder. *Recipes for continuation*, volume 11 of *Comp. Sc. & Eng.* SIAM, 2013. see also <http://sourceforge.net/projects/cocotools/>.
- [DU16] T. Dohnal and H. Uecker. Bifurcation of Nonlinear Bloch waves from the spectrum in the nonlinear Gross-Pitaevskii equation. *J. Nonlinear Sci.*, 26(3):581–618, 2016.
- [DWC⁺14] H. A. Dijkstra, F. W. Wubs, A. K. Cliffe, E. Doedel, I. Dragomirescu, B. Eckhardt, A. Yu. Gelfgat, A. L. Hazel, V. Lucarini, A. G. Salinger, E. T. Phipps, J. Sanchez-Umbria, H. Schuttelaars, L. S. Tuckerman, and U. Thiele. Numerical bifurcation methods and their application to fluid dynamics: Analysis beyond simulation. *Commun. in Comp. Physics*, 15:1–45, 2014.
- [dWDR⁺18] H. de Witt, T. Dohnal, J.D.M. Rademacher, H. Uecker, and D. Wetzel. pde2path - Quickstart guide and reference card, 2018. Available at [Uec18b].
- [EWGT17] S. Engelnkemper, M. Wilczek, S. Gurevich, and U. Thiele. Morphological transitions of sliding drops - dynamics and bifurcations. *Phys-Rev.Fluids*, (1, 073901), 2017.
- [FALD12] G. Formica, A. Arena, W. Lacarbonara, and H. Dankowicz. Coupling FEM with parameter continuation for analysis of bifurcations of periodic responses in nonlinear structures. *Journal of Computational and Nonlinear Dynamics*, 8(2), 2012.
- [FJ91] Th. F. Fairgrieve and A. D. Jepson. O. K. Floquet multipliers. *SIAM J. Numer. Anal.*, 28(5):1446–1462, 1991.
- [GAP06] S. V. Gurevich, Sh. Amiranashvili, and H.-G. Purwins. Breathing dissipative solitons in three-component reaction-diffusion system. *Phys. Rev. E*, 74:066201, 2006.
- [GCF⁺08] D. Grass, J.P. Caulkins, G. Feichtinger, G. Tragler, and D.A. Behrens. *Optimal Control of Nonlinear Processes: With Applications in Drugs, Corruption, and Terror*. Springer, 2008.
- [GF13] S. V. Gurevich and R. Friedrich. Moving and breathing localized structures in reaction-diffusion system. *Math. Model. Nat. Phenom.*, 8(5):84–94, 2013.
- [GKS00] M. Golubitsky, E. Knobloch, and I. Stewart. Target patterns and spirals in planar reaction-diffusion systems. *J. Nonlinear Sci.*, 10(3):333–354, 2000.
- [Gov00] W. Govaerts. *Numerical methods for bifurcations of dynamical equilibria*. SIAM, 2000.
- [GS96] W. Govaerts and A. Spence. Detection of Hopf points by counting sectors in the complex plane. *Numer. Math.*, 75(1):43–58, 1996.
- [GS02] M. Golubitsky and I. Stewart. *The symmetry perspective*. Birkhäuser, Basel, 2002.
- [GU17] D. Grass and H. Uecker. Optimal management and spatial patterns in a distributed shallow lake model. *Electr. J. Differential Equations*, 2017(1):1–21, 2017.
- [Hag82] P.S. Hagan. Spiral waves in reaction-diffusion equations. *SIAM Journal on Applied Mathematics*, 42:762–786, 1982.
- [HH17] A. Hazel and M. Heil. oomph-lib. <http://oomph-lib.maths.man.ac.uk/doc/html>, 2017.
- [HM94] A. Hagberg and E. Meron. Pattern formation in non-gradient reaction-diffusion systems: the effects of front bifurcations. *Nonlinearity*, 7:805–835, 1994.

- [Hoy06] R.B. Hoyle. *Pattern formation*. Cambridge University Press., 2006.
- [KH81] N. Kopell and L.N. Howard. Target pattern and spiral solutions to reaction-diffusion equations with more than one space dimension. *Advances in Applied Mathematics*, 2(4):417–449, 1981.
- [KLS96] Yu.A. Kuznetsov, V.V. Levitin, and A.R. Skovoroda. Continuation of stationary solutions to evolution problems in content. Report AM-R9611, Centrum voor Wiskunde en Informatica, Amsterdam, The Netherlands, 1996.
- [Kno94] E. Knobloch. Bifurcations in rotating systems. In *Lectures on on Solar and Planetary Dynamos, Publications of the Newton Institute, Eds. M.R.E. Proctor and A.D. Gilbert*, pages 247–253. Cambridge University Press, 1994.
- [Kre01] D. Kressner. An efficient and reliable implementation of the periodic qz algorithm. In *IFAC Workshop on Periodic Control Systems*. 2001.
- [Kre06] D. Kressner. A periodic Krylov-Schur algorithm for large matrix products. *Numer. Math.*, 103(3):461–483, 2006.
- [Küh15a] Chr. Kühn. Efficient gluing of numerical continuation and a multiple solution method for elliptic PDEs. *Appl. Math. Comput.*, 266:656–674, 2015.
- [Küh15b] Chr. Kühn. Numerical continuation and SPDE stability for the 2D cubic-quintic Allen-Cahn equation. *SIAM/ASA J. Uncertain. Quantif.*, 3(1):762–789, 2015.
- [Kuz04] Yu. A. Kuznetsov. *Elements of applied bifurcation theory*, volume 112 of *Applied Mathematical Sciences*. Springer-Verlag, New York, third edition, 2004.
- [LR00] K. Lust and D. Roose. Computation and bifurcation analysis of periodic solutions of large-scale systems. In *Numerical methods for bifurcation problems and large-scale dynamical systems (Minneapolis, MN, 1997)*, volume 119 of *IMA Vol. Math. Appl.*, pages 265–301. Springer, New York, 2000.
- [LRSC98] K. Lust, D. Roose, A. Spence, and A. R. Champneys. An adaptive Newton-Picard algorithm with subspace iteration for computing periodic solutions. *SIAM J. Sci. Comput.*, 19(4):1188–1209, 1998.
- [LRTT16] T.S. Lin, S. Rogers, D. Tseluiko, and U. Thiele. Bifurcation analysis of the behaviour of partially wetting liquids on a rotating cylinder. *Phys. Fluids*, 28:082102, 2016.
- [Lus01] K. Lust. Improved numerical Floquet multipliers. *Internat. J. Bifur. Chaos*, 11(9):2389–2410, 2001.
- [Mei00] Z. Mei. *Numerical bifurcation analysis for reaction-diffusion equations*. Springer, 2000.
- [Mie02] A. Mielke. The Ginzburg-Landau equation in its role as a modulation equation. In *Handbook of dynamical systems, Vol. 2*, pages 759–834. North-Holland, 2002.
- [MT04] F. Mazzia and D. Trigiante. A hybrid mesh selection strategy based on conditioning for boundary value ODE problems. *Numerical Algorithms*, 36(2):169–187, 2004.
- [NS15] M. Net and J. Sánchez. Continuation of bifurcations of periodic orbits for large-scale systems. *SIAM J. Appl. Dyn. Syst.*, 14(2):674–698, 2015.
- [Pis06] L.M. Pismen. *Patterns and interfaces in dissipative dynamics*. Springer, 2006.
- [RU17] J.D.M. Rademacher and H. Uecker. Symmetries and freezing of 1D problems in pde2path – a tutorial via some Ginzburg-Landau and FHN models, 2017. Available at [Uec18b].
- [Sal16] A. Salinger. LOCA. www.cs.sandia.gov/LOCA/, 2016.
- [Sch98] A. Scheel. Bifurcation to spiral waves in reaction-diffusion systems. *SIAM journal on mathematical analysis*, 29(6):1399–1418, 1998.
- [SDE⁺15] E. Siero, A. Doelman, M. B. Eppinga, J. D. M. Rademacher, M. Rietkerk, and K. Siteur. Striped pattern selection by advective reaction-diffusion systems: resilience of banded vegetation on slopes. *Chaos*, 25(3), 2015.

- [Sey10] R. Seydel. *Practical bifurcation and stability analysis. 3rd ed.* Springer, 2010.
- [SGN13] J. Sánchez, F. Garcia, and M. Net. Computation of azimuthal waves and their stability in thermal convection in rotating spherical shells with application to the study of a double-hopf bifurcation. *Phys. Rev. E*, page 033014, 2013.
- [SN10] J. Sánchez and M. Net. On the multiple shooting continuation of periodic orbits by newton-krylov methods. *Int. J. Bifurcation and Chaos*, 20(1):43–61, 2010.
- [SN16] J. Sánchez and M. Net. Numerical continuation methods for large-scale dissipative dynamical systems. *Eur. Phys. J. Special Topics*, 225:2465–2486, 2016.
- [SNGAS04] J. Sánchez, M. Net, B. García-Archilla, and C. Simó. Newton-Krylov continuation of periodic orbits for Navier-Stokes flows. *J. Comput. Phys.*, 201(1):13–33, 2004.
- [SS07] B. Sandstede and A. Scheel. Period-doubling of spiral waves and defects. *SIAM J. Appl. Dyn. Syst.*, 6(2):494–547, 2007.
- [SSW99] B. Sandstede, A. Scheel, and C. Wulff. Bifurcations and dynamics of spiral waves. *J. Nonlinear Sci.*, 9(4):439–478, 1999.
- [Tau15] N. Tauchnitz. The Pontryagin maximum principle for nonlinear optimal control problems with infinite horizon. *J. Optim. Theory Appl.*, 167(1):27–48, 2015.
- [TB00] L. S. Tuckerman and D. Barkley. Bifurcation analysis for timesteppers. In *Numerical methods for bifurcation problems and large-scale dynamical systems (Minneapolis, MN, 1997)*, volume 119 of *IMA Vol. Math. Appl.*, pages 453–466. Springer, New York, 2000.
- [Tsa10] Je-Chiang Tsai. Rotating spiral waves in λ - ω systems on circular domains. *Physica D*, 239:1007–1025, 2010.
- [TW96] O. Tahvonon and C. Withagen. Optimality of irreversible pollution accumulation. *Journal of Environmental Economics and Management*, 20:1775–1795, 1996.
- [Uec16] H. Uecker. Optimal harvesting and spatial patterns in a semi arid vegetation system. *Natural Resource Modelling*, 29(2):229–258, 2016.
- [Uec17] H. Uecker. Infinite time-horizon spatially distributed optimal control problems with pde2path – a tutorial, 2017. Available at [Uec18b].
- [Uec18a] H. Uecker. User guide on Hopf bifurcation and time periodic orbits with pde2path, 2018. Available at [Uec18b].
- [Uec18b] H. Uecker. www.staff.uni-oldenburg.de/hannes.uecker/pde2path, 2018.
- [UW14] H. Uecker and D. Wetzel. Numerical results for snaking of patterns over patterns in some 2D Selkov-Schnakenberg Reaction-Diffusion systems. *SIADS*, 13-1:94–128, 2014.
- [UW17] H. Uecker and D. Wetzel. The pde2path linear system solvers – a tutorial, 2017. Available at [Uec18b].
- [UWR14] H. Uecker, D. Wetzel, and J.D.M. Rademacher. pde2path – a Matlab package for continuation and bifurcation in 2D elliptic systems. *NMTMA*, 7:58–106, 2014.
- [VE01] V. K. Vanag and I. R. Epstein. Inwardly rotating spiral waves in a reaction-diffusion system. *Science*, 294, 2001.
- [Wet16] D. Wetzel. Pattern analysis in a benthic bacteria-nutrient system. *Math. Biosci. Eng.*, 13(2):303–332, 2016.
- [WJ13] I. Waugh, S. Illingworth, and M. Juniper. Matrix-free continuation of limit cycles for bifurcation analysis of large thermoacoustic systems. *J. Comput. Phys.*, 240:225–247, 2013.
- [Wir96] Fr. Wirl. Pathways to Hopf bifurcation in dynamic, continuous time optimization problems. *Journal of Optimization Theory and Applications*, 91:299–320, 1996.

- [Wir00] Fr. Wirl. Optimal accumulation of pollution: Existence of limit cycles for the social optimum and the competitive equilibrium. *Journal of Economic Dynamics and Control*, 24(2):297–306, 2000.
- [YDZE02] L. Yang, M. Dolnik, A. M. Zhabotinsky, and I. R. Epstein. Pattern formation arising from interactions between Turing and wave instabilities. *J. Chem. Phys.*, 117(15):7259–7265, 2002.
- [YE03] L. Yang and I. R. Epstein. Oscillatory Turing patterns in reaction–diffusion systems with two coupled layers. *PRL*, 90(17):178303–1–4, 2003.
- [ZHKR15] D. Zhelyazov, D. Han-Kwan, and J. D. M. Rademacher. Global stability and local bifurcations in a two-fluid model for tokamak plasma. *SIAM J. Appl. Dyn. Syst.*, 14(2):730–763, 2015.
- [ZUFM17] Y. Zelnik, H. Uecker, U. Feudel, and E. Meron. Desertification by front propagation? *Journal of Theoretical Biology*, pages 27–35, 2017.